

In: "Nanoelectronics and Information Technology"

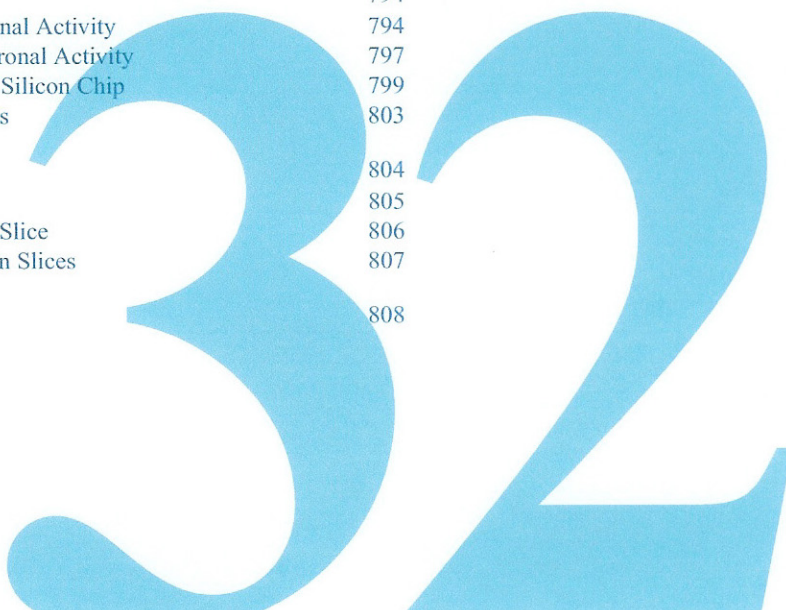
Editor: Rainer Waser, Wiley-VCH (Berlin, 2003), 781-810.

# Neuroelectronic Interfacing: Semiconductor Chips with Ion Channels, Nerve Cells, and Brain

*Peter Fromherz,*

*Max Planck Institute for Biochemistry, Department of Membrane and Neurophysics,  
Martinsried, Germany*

<b>1 Introduction</b>	783
<b>2 Iono-Electronic Interface</b>	784
2.1 Planar Core-Coat Conductor	784
2.2 Cleft of Cell-Silicon Junction	786
2.3 Conductance of the Cleft	789
2.4 Ion Channels in Cell-Silicon Junction	792
<b>3 Neuron-Silicon Circuits</b>	794
3.1 Transistor Recording of Neuronal Activity	794
3.2 Capacitive Stimulation of Neuronal Activity	797
3.3 Circuits with Two Neurons on Silicon Chip	799
3.4 Towards defined Neuronal Nets	803
<b>4 Brain-Silicon Chips</b>	804
4.1 Tissue-Sheet Conductor	805
4.2 Transistor Recording of Brain Slice	806
4.3 Capacitive Stimulation of Brain Slices	807
<b>5 Summary and Outlook</b>	808





# Neuroelectronic Interfacing: Semiconductor Chips with Ion Channels, Nerve Cells, and Brain

## 1 Introduction

Computers and brains both work electrically. However, their charge carriers are different – electrons in a solid ion lattice and ions in a polar fluid. Electrons in silicon have a mobility of about  $10^3 \text{ cm}^2/\text{Vs}$ , whereas the mobility of ions in water is around  $10^{-3} \text{ cm}^2/\text{Vs}$ . That enormous difference of mobility is at the root for the different architecture of the two information processors. It is an intellectual and technological challenge to join these different systems directly on the level of electronic and ionic signals as sketched in Figure 1.

In the 18<sup>th</sup> century, Luigi Galvani established the electrical coupling of inorganic solids and excitable living tissue. Now, after fifty years of dramatic developments in semiconductor microtechnology and cellular neurobiology, we may envisage such an integration by far more complex interactions, right on the level of individual nerve cells and microelectronic devices or even on the level of biomolecules and nanostructures. Today, however, we are not concerned whether brain-computer interfacing can be really implemented in the foreseeable future, with neuronal dynamics and digital computation fused to thinking-computing systems. The issue is an elucidation of the fundamental biophysical mechanisms on the level of nanometers, micrometers and millimeters, and the development of a scientific and technological culture that combines the theoretical concepts and experimental methods of microelectronics, solid state physics, electrochemistry, molecular biology and neurobiology. If we succeed in that endeavour, then we shall be able to fabricate ionoelectronic devices to solve problems in molecular biology, to develop neuroelectronic devices for an experimental physics of brain-like systems, and to contribute to medicine and information technology by creating microelectronic neuroprostheses and nerve-based ionic processors.

Having worked for some time with artificial biomembranes on semiconductor electrodes, I wrote in 1985 a note “Brain on line? The feasibility of a neuron-silicon-junction” [1]. The idea of brain-computer interfacing was scaled down to the level of a real project: “The utopian question may be shaped into a proper scientific problem: How to design a neuron-silicon junction?” I outlined the mechanism of neuron-semiconductor interfacing in both directions. On that basis, the first experimental results were reported in 1991 and 1995 with nerve cells of the leech on open transistors and on capacitive stimulation spots of silicon chips [2], [3]. After those elementary steps, two directions were followed: (i) Downwards, the microscopic nature of the cell-semiconductor contact was investigated with respect to its structure and electrical properties [4] – [23]. The goal is a physical rationalization of the junction in order to have a firm basis for a systematic optimization of neuron-silicon interfacing [24] – [29]. (ii) Upwards, hybrid systems were assembled with neuronal networks joined to microelectronic circuits [30] – [41]. Here the goal is a supervision of numerous neurons in a network by noninvasive contacts to a semiconductor substrate as required for long term studies of dynamical processes such as learning and memory.

The present article relies on own publications [2] – [41] and reviews [42] – [45]. It discusses the physics of the cell-silicon junction, the electronic interfacing of individual neurons by transistor recording and capacitive stimulation, and first steps towards a connection of silicon chips with neuronal networks and with brain slices. Literature on the background of the field is found in the reference lists of the original publications.

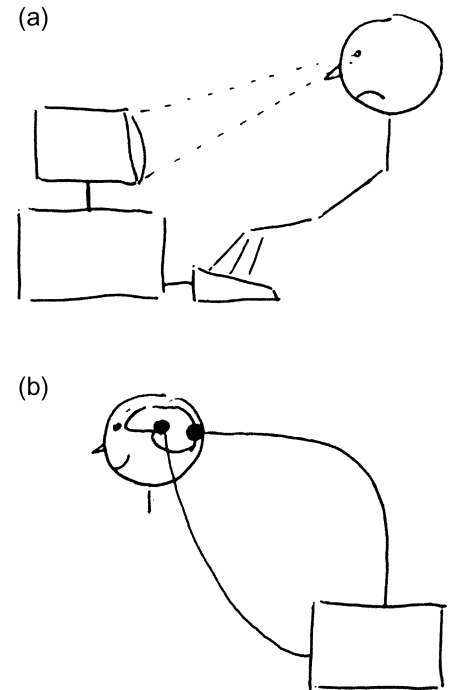


**Figure 1:** Cartoon of brain-computer interfacing. (a) Communication through the macroscopic optical and mechanical pathways screen-eye and finger-keyboard. (b) Hypothetical microscopic interfacing of a computer with the visual and motor cortex [1].

## 2 Iono-Electronic Interface

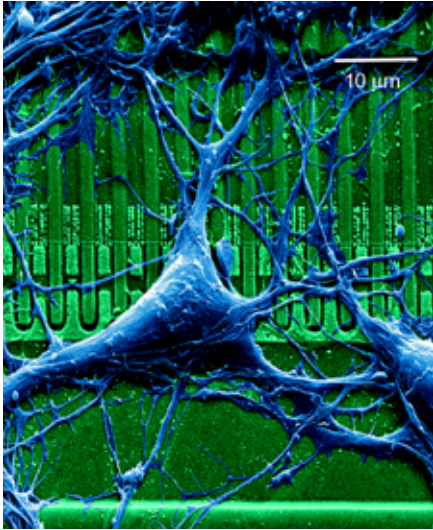


**Figure 2:** Nerve cell from a rat brain on a silicon chip [22]. Colored electron micrograph, scale bar 10  $\mu\text{m}$ . The surface of the chip consists of thermally grown silicon dioxide (green). The metal free gates of a linear array of field-effect transistors are visible as dark squares. The neuron (blue) is cultured on the chip for several days in an electrolyte.

A neuron-silicon chip with an individual nerve cell from rat brain and a linear array of transistors is shown in Figure 2. A nerve cell (diameter about 20  $\mu\text{m}$ ) is surrounded by a membrane with an electrically insulating core of lipid. That lipid bilayer (thickness about 5 nm) separates the environment with about 150 mM ( $10^{20} \text{ cm}^{-3}$ ) sodium chloride from the intracellular electrolyte with about 150 mM potassium chloride. Ion currents through the membrane are mediated by specific protein molecules, ion channels with a conductance between 10 pS and 100 pS. Silicon is used as an electronically conductive substrate for three reasons: (i) Coated with a thin layer of thermally grown silicon dioxide (thickness 10 - 1000 nm), silicon is a perfect inert substrate for culturing nerve cells. (ii) The thermally grown silicon dioxide suppresses the transfer of electrons and the concomitant electrochemical processes that lead to a corrosion of silicon and to a damage of the cells. (iii) A well established semiconductor technology allows the fabrication of microscopic electronic devices that are in direct contact to the cells, shielded by the inert oxide layer.

In principle, a direct coupling of ionic signals in a neuron and electronic signals in the semiconductor can be attained by electrical polarization. If the insulating lipid layer of the neuron is in direct contact to the insulating silicon dioxide of the chip, a compact dielectric is formed as sketched in Figure 3a and Figure 3b. An electrical field across the membrane – as created by neuronal activity – polarizes the silicon dioxide such that the electronic band structure of silicon and an integrated transistor is affected (Figure 3a). Vice versa, an electrical field across the silicon dioxide – as caused by a voltage applied to the chip – polarizes the membrane in a way that conformations of field-sensitive membrane proteins such as voltage-gated ion channels are affected (Figure 3b).

However, when a nerve cell grows on a chip as illustrated in Figure 2, we cannot expect, that the lipid layer of the cell and the oxide layer of silicon form a compact dielectric. Cell adhesion is mediated by protein molecules that protrude from the cell membrane (integrins, glycocalix) and that are deposited on the substrate (extracellular matrix proteins). These proteins keep the lipid core of the membrane at a certain distance from the substrate, stabilizing a cleft between cell and chip that is filled with electrolyte as indicated in Figure 3c and Figure 3d. The conductive cleft shields electrical fields and suppresses a direct mutual polarization of silicon dioxide and membrane.

The cell-silicon junction forms a planar electrical core-coat conductor: the coats of silicon dioxide and membrane insulate the core of the conductive cleft from the conducting environments of silicon and cytoplasm. The first step of neuroelectronic interfacing is determined by the current flow in that core-coat conductor [10], [26]: (i) The activity of a neuron leads to ionic and displacement currents through the membrane (Figure 3c). The concomitant current along the core gives rise to a *Transductive Extracellular Potential (TEP)* between cell and chip. (ii) A voltage transient applied to silicon leads to a displacement current through the oxide coat (Figure 3d). Again a *Transductive Extracellular Potential* appears between chip and cell due to the concomitant current along the cleft. In a second step of interfacing, the *Transductive Extracellular Potential* in the core-coat conductor is detected by voltage-sensitive devices in the chip or in the cell: (i) The *TEP* induced by the neuron gives rise to an electrical field across the silicon dioxide that is probed by a field-effect transistor (Figure 3c). (ii) The *TEP* induced by the chip gives rise to an electrical field across the membrane that is probed by voltage-gated ion channels (Figure 3d).

### 2.1 Planar Core-Coat Conductor

The *Transductive Extracellular Potential* mediates the coupling of neurons and silicon. It is determined by the current balance in the core-coat conductor of the junction [10]. To describe current and voltage, we use the two-dimensional area-contact model or the zero-dimensional point-contact model as sketched in Figure 4.

**Area-contact model.** We describe the current in each area element of the junction by the area-contact model symbolized by the circuit of Figure 4a [10], [14]. The current along the cleft is balanced by the displacement current through silicon dioxide and by the ionic and displacement current through the attached membrane. The conservation of electrical charge per unit area of the junction is expressed by (1) where the left hand side refers to the balance of current per unit length in the cleft and the right hand side to the current per unit area through membrane and oxide with the electrical potential  $V_M$  in the cell (membrane potential), the potential  $V_S$  in the substrate, the *Transductive Extracellular*

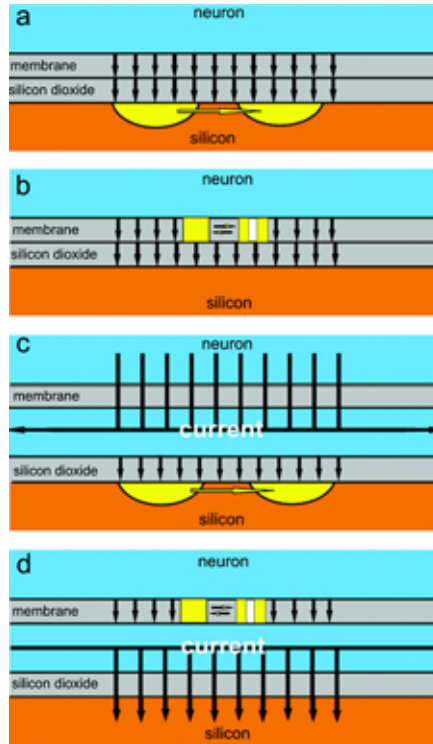


**Figure 3:** Iono-electronic interfacing. Schematic cross sections, not to scale.

(a) and (b) direct polarization of cell and chip. In (a) the electrical field in the membrane of an excited neuron polarizes silicon dioxide and modulates the source-drain current of a transistor (yellow: source and drain). In (b) an electrical field in silicon dioxide polarizes the membrane and opens ion channels (yellow: closed and open conformations).

(c) and (d) neuron-silicon coupling by electrical current. In (c) current through the membrane of an excited neuron leads to a *Transductive Extracellular Potential* in the cleft between cell and chip which polarizes the oxide and modulates the source-drain current. In (d) capacitive current through the oxide gives rise to a *Transductive Extracellular Potential*, which polarizes the membrane and opens ion channels.

Potential  $V_J$  in the junction and the two-dimensional spatial derivative operator  $\nabla$ . If the bath electrolyte is kept on ground potential ( $V_E = 0$ ),  $V_M$ ,  $V_S$  and  $V_J$  are the voltages between cell, silicon and junction and the bath.

$$-\nabla \left( \frac{1}{r_J} \nabla V_J \right) = c_S \left( \frac{\partial V_S}{\partial t} - \frac{\partial V_J}{\partial t} \right) + c_M \left( \frac{\partial V_M}{\partial t} - \frac{\partial V_J}{\partial t} \right) + g_{JM} (V_M - V_J) \quad (1)$$

Parameters are the sheet resistance of the cleft, the area specific capacitances  $c_M$  and  $c_S$  of membrane and substrate and an area specific leak conductance  $g_{JM}$  of the attached membrane. Voltage-dependent ion conductances are not included in (1), for sake of clarity. The specific capacitance  $c_M$  in the attached membrane is assumed to be the same as in the free membrane. The sheet resistance  $r_J$  can be expressed by the width  $d_J$  and the specific resistance  $\rho_J$  of the cleft  $r_J$  with  $r_J = \rho_J/d_J$

**Point-contact model.** For many applications it is convenient to describe the core-coat conductor by an equivalent circuit shown in Figure 4b [9], [10], [26]. The conductive cleft is represented by a global Ohmic conductance  $G_J$ , attached membrane and silicon dioxide by the global capacitances  $C_{JM}$  and  $C_S$ . We take into account global ion specific conductances  $G_{JM}^i$  in the attached membrane. The reversal voltages  $V_0^i$  originate in the concentration differences of the ions between cell and environment, which flow through the conductances  $G_{JM}^i$ . They are assumed to be the same as in the free membrane. When we define area specific parameters with respect to the area  $A_{JM}$  of the attached membrane as  $c_S = C_S/A_{JM}$ ,  $c_M = C_{JM}/A_{JM}$ ,  $g_{JM}^i = G_{JM}^i/A_{JM}$  and  $g_J = G_J/A_{JM}$ , Kirchoff's law is expressed by (2) where  $V_J$  and  $V_E$  are the potentials in the junction and in the bulk electrolyte.

$$g_J (V_J - V_E) = c_S \left( \frac{dV_S}{dt} - \frac{dV_J}{dt} \right) + c_M \left( \frac{dV_M}{dt} - \frac{dV_J}{dt} \right) + \sum_i g_{JM}^i (V_M - V_J - V_0^i) \quad (2)$$

**Electrodiffusion.** The area-contact and the point-contact model as expressed by (1) and (2) imply that the ion concentrations in the narrow cleft between cell and chip are not changed with constant  $r_J$ , constant  $g_J$  and constant  $V_0^i$ . A change of the ion concentrations in the cleft may become important when the density of ion channels in the junction is high and when these channels are open for an extended time interval. An electrodiffusion version of the area-contact and of the point-contact model accounts for these effects [11].

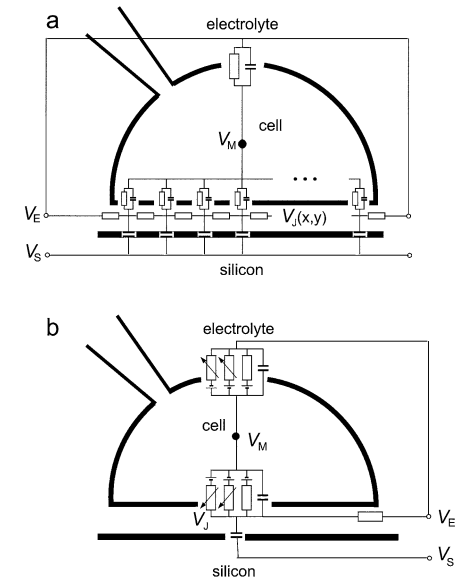


**Figure 4:** Core-coat conductor of cell-semiconductor junction [10], [26]. The heavy lines indicate silicon dioxide, cell membrane and micropipette. The cross sections are not to scale: the distance of membrane and chip is between 10 nm and 100 nm, the diameter of a cell is between 10  $\mu\text{m}$  and 100  $\mu\text{m}$ .

(a) AC circuit of area-contact model. The infinitesimal elements of oxide, membrane and electrolyte film in the junction are represented as capacitors and Ohmic resistances.

(b) DC circuit of point-contact model with voltage-dependent ion conductances. Oxide, membrane and electrolyte film of the junction are represented by global capacitances and resistances.  $V_M$  is the electrical potential in the cell,  $V_J$  the *Transductive Extracellular Potential* in the junction,  $V_S$  the potential of the substrate and  $V_E$  the potential of the bath.

**Area-contact vs. point-contact.** A comparison of (1) and (2) shows that the Laplace operator in a homogeneous area-contact model is replaced by a constant in the point-contact model with  $-\nabla^2 \rightarrow r_j g_j$ . To match the two models, we must express the area specific conductance  $g_j = G_j/A_{JM}$  by the sheet resistance  $r_j$ . Various averaging methods lead to a relation  $G_j^{-1} = r_j/\theta\pi$  between global resistance and sheet resistance with a scaling factor  $\theta = 4 - 6$  [10], [12], [13]. For a circular junction of radius  $a_j$  with  $A_{JM} = a_j^2\pi$ , we obtain (3) with  $r_j = \rho_j/d_j$ .

$$g_j = \theta \frac{1}{r_j a_j^2} = \theta \frac{d_j}{\rho_j a_j^2} \quad (3)$$

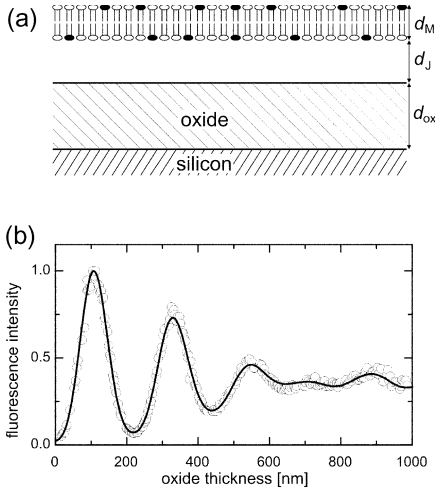


**Figure 5:** Fluorescent lipid membrane on silicon [5]. (a) Schematic cross section of lipid bilayer with incorporated dye molecules on oxidized silicon. The distance of membrane and chip is  $d_j$ , the thickness of the oxide is  $d_{ox}$ . (b) Experimental fluorescence intensity of a bilayer with the cyanine dye DiI versus oxide thickness. The data are fitted by the electromagnetic theory of dipole radiation with a single free parameter, the scaling factor of intensity.

Area specific parameters are preferred in the point-contact model, because a single parameter  $g_j$  combines three unknown properties of the junction – the specific resistance  $\rho_j$ , the width  $d_j$  and the radius  $a_j$ , because the area specific capacitances  $c_M$  and  $c_S$  of membrane and chip are usually known and because area specific membrane conductances  $g_{JM}^i$  are common in the neurophysiological literature.

**Intracellular dynamics.** The *Transductive Extracellular Potential*  $V_J$  is determined by the current in the junction alone (1), (2), if the potentials  $V_M$  and  $V_S$  in cell and chip are under external control. Usually that condition holds for the chip, where  $V_S$  is held constant or is determined by a waveform  $V_S(t)$  of stimulation. For the cell,  $V_M$  is held constant in voltage-clamp situations when the intracellular space is controlled by a micropipette (Figure 4). In situations of noninvasive extracellular recording and stimulation by a chip, the intracellular potential  $V_M(t)$  obeys an autonomous dynamics, governed by the balance of ionic and displacement currents through the free and attached membrane as indicated in Figure 4.

For the point-contact model we obtain (4) using Kirchoff's law, where the left hand side describes the outward current through the free membrane, and the right hand side refers to the inward current through the attached membrane with the area specific ion conductances  $g_{JM}^i$  and  $g_{FM}^i$  of attached and free membrane and with the ratio  $\beta_M = A_{JM}/A_{FM}$  of attached and free membrane area.

$$\begin{aligned} c_M \left( \frac{dV_M}{dt} - \frac{dV_E}{dt} \right) + \sum_i g_{FM}^i (V_M - V_E - V_0^i) \\ = -\beta_M \left[ c_M \left( \frac{dV_M}{dt} - \frac{dV_J}{dt} \right) + \sum_i g_{JM}^i (V_M - V_J - V_0^i) \right] \end{aligned} \quad (4)$$

(2) and (4) together describe the coupled dynamics of the intracellular and extracellular potentials  $V_M(t)$  and  $V_J(t)$  for the point-contact model. In analogy, the area-contact model has to be amended by the intracellular dynamics. There, Kirchoff's law for the cell is given by the outward current through the free membrane as given by the left hand side of (4) and by an integral over all local inward currents through the attached membrane area [13].

**Conclusion.** The interfacing of neuron and semiconductors is mediated by a *Transductive Extracellular Potential*. A large *TEP* results from high currents through membrane and silicon dioxide, and from a low conductance of the junction. Recording and stimulation of neuronal activity are promoted by a small distance  $d_j$ , a high specific resistance  $\rho_j$ , and a large radius  $a_j$  of the cell-chip junction. Efficient recording requires high ion conductances  $g_{JM}^i$  in the attached membrane, efficient stimulation a high area specific capacitance  $c_S$  of the chip.

## 2.2 Cleft of Cell-Silicon Junction

The distance  $d_j$  between a cell membrane and a silicon chip is a fundamental parameter of cell-silicon junctions. The distance is measured by the method of fluorescence interference contrast (*FLIC*) microscopy which relies on the formation of standing modes of light in front of the reflecting surface of silicon.

**Fluorescence on silicon.** We consider a lipid bilayer on oxidized silicon as sketched in Figure 5a. The membrane is labelled with amphiphilic dye molecules with transition dipoles in the membrane plane. Upon illumination, light is reflected at all interfaces, in

particular at the interface silicon to silicon dioxide. Also the fluorescence light emitted by the dye molecules is reflected. Due to interference effects the excitation and the fluorescence of the dye depend on the distance between membrane and silicon [4].

The electrical field of a light wave has a node in the plane of an ideal mirror. For normal incidence of light, the probability of excitation of a membrane-bound dye is described by the first factor of (5) with a thickness  $d_{ox}$  and a refractive index  $n_{ox}$  of silicon dioxide, with a width  $d_j$  and refractive index  $n_j$  of the cleft between membrane and chip and with a wavelength  $\lambda_{ex}$ . An analogous interference effect occurs for light that is emitted from the dye directly and with reflection. The probability of fluorescence at a wavelength  $\lambda_{em}$  in normal direction is described by the second factor of (5). The detected stationary fluorescence intensity  $J_{fl}(d_j, d_{ox})$  is proportional to the product of excitation and emission probability according to (5) [4] which can be read as a function  $J_{fl}(d_j)$  at constant  $d_{ox}$  or as a function  $J_{fl}(d_{ox})$  at constant  $d_j$ .

$$J_{fl}(d_j, d_{ox}) \propto \sin^2 \left[ \frac{2\pi(n_{ox}d_{ox} + n_j d_j)}{\lambda_{ex}/2} \right] \cdot \sin^2 \left[ \frac{2\pi(n_{ox}d_{ox} + n_j d_j)}{\lambda_{em}/2} \right]. \quad (5)$$

For a cell on silicon, the complete electromagnetic theory of dipole radiation has to be applied. It leads to a more involved function  $J_{fl}(d_{ox}, d_j)$  which takes into account the layered optical structure, the aperture of a microscope, the spectral bandwidth of illumination and detection and the nearfield interaction of dye and silicon [5].

For an experimental test of the modulated fluorescence on silicon, we attach ( $d_j \approx 0$ ) a pure lipid bilayer with the cyanine dye DiI to a silicon chip with 256 terraces of silicon dioxide. The observed fluorescence intensity  $J_{fl}(d_{ox})$  is plotted in Figure 5b. We observe a damped periodic variation of the intensity which levels out above 600 nm due to the large aperture and the wide spectral bandwidth of detection. The experiment is perfectly fitted with the relation  $J_{fl}(d_{ox})$  of the complete electromagnetic theory using a single free parameter, the scaling factor of the intensity [5].

**FLIC microscopy.** The modulation of fluorescence on silicon is the basis of *FLIC* microscopy which allows to determine the distance between a chip and a cell. A direct evaluation of  $d_j$  from the measured fluorescence intensity and the theoretical function  $J_{fl}(d_{ox}, d_j)$  at a given value  $d_{ox}$  is not possible (i) because we cannot measure absolute intensities [4] and (ii) because there is a background fluorescence from the upper membrane of the cell out of focus [6]. To overcome that problem, the intensity  $J_{fl}(d_{ox}, d_j)$  of the membrane is measured on several oxide layers of different height  $d_{ox}$  at a certain unknown value of  $d_j$ . Usually 4 or 16 quadratic terraces are fabricated in a  $10 \mu\text{m} \times 10 \mu\text{m}$  unit cell of the silicon surface [6], [7]. The data are fitted by a function  $\tilde{J}_{fl}$  according to (6) with three parameters, a scaling factor  $a$ , a background  $b$  and the optical width of the cleft  $n_j d_j$ .

$$\tilde{J}_{fl} = aJ_{fl}(d_{ox}, d_j) + b \quad (6)$$

It is a main advantage of *FLIC* microscopy that the theoretical function  $J_{fl}(d_{ox}, d_j)$  is dominated by the optics of the well defined interface of silicon and silicon dioxide. Not well known optical parameters of the cell – the thickness of the membrane including protein complexes and the refractive indices of membrane and cytoplasm – play almost no role. Prerequisite of *FLIC* microscopy is a similar geometry of cell adhesion on the different terraces and a homogeneous staining of the membrane.

**Astrocyte on laminin.** A fluorescence micrograph of a glia cell from rat brain (astrocyte) on 16 different terraces is shown in Figure 6a. The chip is coated with a protein from the extracellular matrix (laminin) with a thickness of 3 nm in its dry state. The checkerboard pattern of fluorescence matches the oxide terraces [6]. Two features of the picture are important: (i) The intensity is rather homogeneous on each terrace. (ii) The intensity is periodic with the unit cells of  $4 \times 4$  terraces. These observations indicate that the membrane is stained homogeneously and that a well defined distance of membrane and chip exists on all terraces.

The fluorescence intensity  $J_{fl}^{exp}(d_{ox})$  on 16 terraces is plotted in Figure 6b versus the height of the terraces. It is highest on the thinnest oxide, drops and increases again on higher terraces. That result is quite in contrast to the model experiment of Figure 5b. For comparison, the result of a control experiment is plotted in Figure 6b where a stained vesicle made of a pure lipid bilayer is attached to the same microscopic terraces with polylysine and observed under the same optical conditions [16]. There the fluorescence starts with a minimum on the thinnest oxide as in the model experiment with a

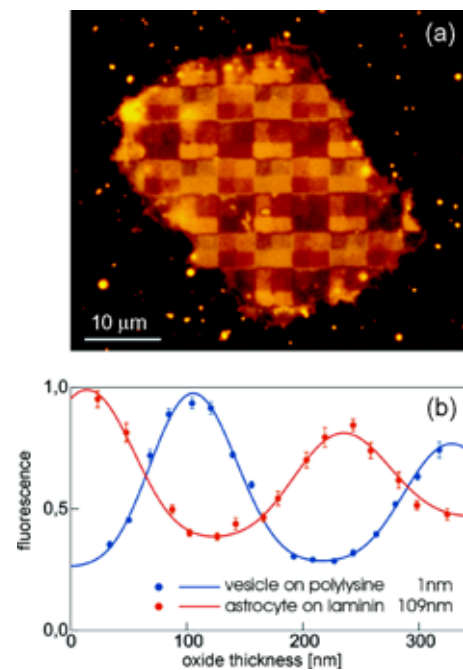


**Figure 6:** Fluorescence interference contrast (*FLIC*) microscopy of astrocyte [7].

(a) Fluorescence micrograph of the adhesion region of a rat astrocyte on a silicon chip with quadratic  $2.5 \mu\text{m} \times 2.5 \mu\text{m}$  terraces of silicon dioxide. Scale bar  $10 \mu\text{m}$ . The chip is coated with laminin. The membrane is stained with the dye *DiI*.

(b) Fluorescence intensity versus height of the terraces for the astrocyte (red dots) and a lipid vesicle on polylysine (blue dots). The lines are computed by an electromagnetic theory assuming a water film between oxide and membrane of 109 nm thickness for the astrocyte and of 1 nm for the lipid vesicle.

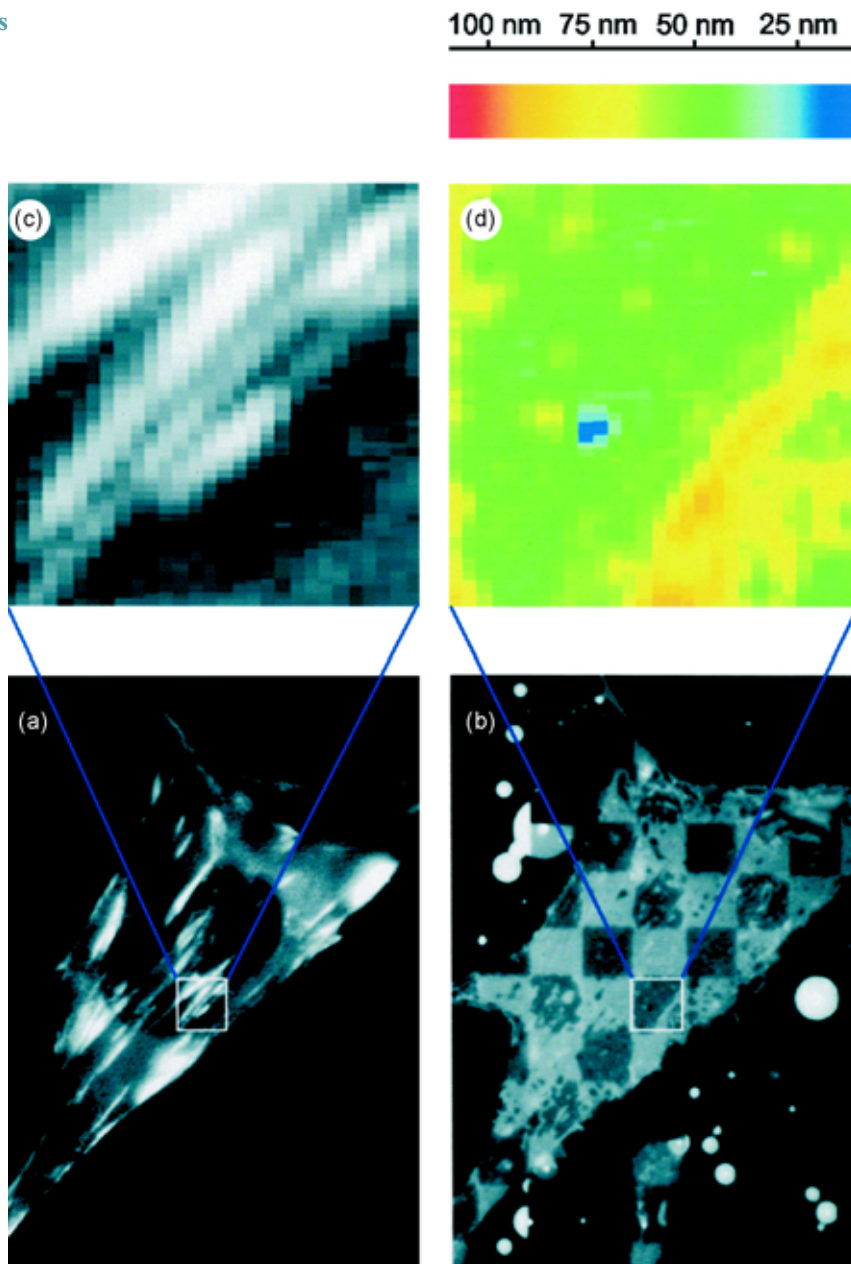


**Figure 7:** Focal contact of fibroblast on fibronectin [8].  
 (a) Fluorescence micrograph in the light of *GFP* (*green fluorescent protein*) fused to vinculin showing elongated focal contacts.  
 (b) *FLIC* micrograph in the light of the cyanine dye *DiI*. The size of the four terraces of different height is  $5\ \mu\text{m} \times 5\ \mu\text{m}$ .  
 (c) Blow up of a terrace of the vinculin picture.  
 (d) Color coded map of the distance between cell and chip obtained by *FLIC* microscopy on the selected terrace. Within the lateral resolution of about 400 nm, there is no close contact in correlation to the areas of focal adhesion.

planar lipid bilayer Figure 5. A fit of the data according to (6) leads to  $d_1 = 1\ \text{nm}$  assuming a refractive index of water. On the other hand, a fit of the data for the astrocyte membrane on laminin leads to  $d_1 = 109\ \text{nm}$ .

**Focal contact.** For comparison we consider fibroblast cells on the extracellular matrix protein fibronectin. Their special cellular structures promote strong adhesive forces such that we may expect a particularly close distance of cell and chip. We visualize these focal contacts by fusing *green fluorescent protein* (*GFP*) to vinculin, one of their protein components, as shown in Figure 7a [8]. Choosing a different illumination we perform a *FLIC* experiment with the cyanine dye *DiI* on a chip with four different terraces as shown in Figure 7b. For a selected terrace depicted in Figure 7c, we compute a distance map  $d_1(x,y)$ . Figure 7d shows that even at focal contacts with their strong adhesion, the separation of the lipid core of the cell membrane and the chip is 50 nm within the lateral resolution of the microscope.

**Conclusion.** The lipid core of a cell membrane and the silicon dioxide layer of a silicon chip are not in close contact. The large distance is caused by dangling polymer molecules that protrude from the membrane (glycocalix) and that are deposited on the chip (laminin) [17]. They give rise to repulsive entropic forces that balance the attractive forces of cell adhesion between the integrins in the membrane and laminin molecules. It will be an important task to lower the distance of cells and chips by special treatments of the chip surface and by genetic modifications of the membrane without impairing the viability of the cells.

### 2.3 Conductance of the Cleft

Given a cleft between cell and chip, we have to ask for the sheet resistance  $r_j$  of the junction in the area-contact model or for the area specific conductance  $g_j$  in the point-contact model. Various approaches can be chosen to obtain  $r_j$  or  $g_j$  from measurements of the voltage transfer in the junction, considering the circuits of Figure 4: (i) We may apply a voltage  $V_M - V_E$  between cell and bath [9] - [15] or a voltage  $V_S - V_E$  between chip and bath [15], [16], [21]. (ii) We may probe the voltage drop  $V_J - V_S$  across the oxide with field-effect transistors [9] - [14], [15], [16] or the voltage  $V_M - V_J$  across the membrane with voltage-sensitive dye [16]. (iii) We may use ac voltages [9] - [16] or voltage steps [21] for stimulation. (iv) We may use the point-contact model [9], [10], [15] or the area-contact model [10], [15] to evaluate the data. After considering the nature of transistor recording, we discuss here an intracellular ac stimulation with transistor recording evaluated by the point-contact model, and an extracellular ac stimulation with transistor recording evaluated by the area-contact model. Finally, we describe an extracellular pulse stimulation with optical recording by a voltage-sensitive dye.

**Transistor recording.** In a p-type *metal oxide silicon field effect transistor (MOSFET)* the source-drain current  $I_D$  is controlled by the voltage  $V_{DS}$  between drain and source and the voltage  $V_{GS}$  between metal gate and source. Above the threshold  $V_{GS} > V_T$  of strong inversion and below pinch-off, the current is described by (7) where the proportionally constant depends on the length and width of the channel, the mobility of the holes and the capacitance of the gate oxide.

$$I_D \propto [V_{DS}(V_{GS} - V_T) - V_{DS}^2/2] \quad (7)$$

An electrolyte replaces the metal gate in an *electrolyte oxide silicon field effect transistor (EOSFET)*. It is joined to an external metallic contact by a Ag/AgCl electrode that transforms ionic into electronic current. The source-drain current is controlled by the voltage  $V_{ES} = V_E - V_S$  applied to the electrolyte. In (7) we substitute  $V_{GS} \rightarrow V_{ES}$  and  $V_T \rightarrow V_T^{(E)}$  where the threshold  $V_T^{(E)}$  is determined by the work function of silicon, the redox potential of Ag/AgCl, the contact potential of the Ag/AgCl electrode and the electrical double layer at the interface electrolyte / silicon dioxide.

When we probe the electrical effect of a cell, the source-drain current of an *EOSFET* is modulated by the voltage  $V_{JS} = V_J - V_S$  in the cell-silicon junction, of course. The cell affects the voltage drop  $V_{JE} = V_J - V_E$  between junction and bulk electrolyte at a constant external voltage  $V_{ES}$ . With  $V_{JS} = V_{JE} + V_{ES}$  we obtain for transistor recording (8).

$$I_D \propto [V_{DS}(V_{JE} + V_{ES} - V_T^{(E)}) - V_{DS}^2/2] \quad (8)$$

The change of the extracellular potential occurs in the cleft between cell and chip, far beyond the electrical double layer which has a thickness of 1 nm in 100 mM NaCl. Thus we are dealing with a genuine modulation of the gate voltage. Local voltage recording by an *EOSFET* has to be distinguished from the application of an *EOSFET* as an *ion-sensitive transistor (ISFET)*. There molecular interactions of protons and other ions in the electrical double layer modulate the threshold voltage  $V_T^{(E)}$ .

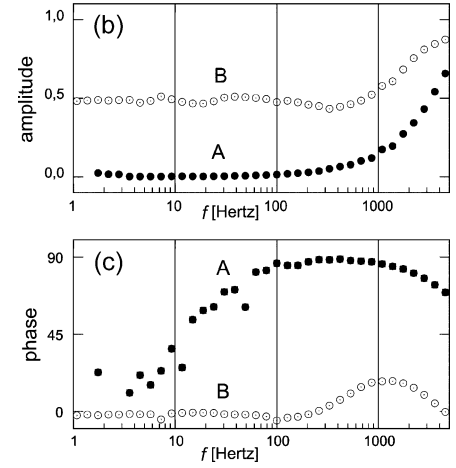
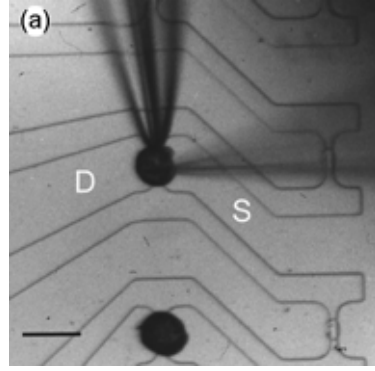
The characteristics  $I_D(V_{DS}, V_{ES})$  of an *EOSFET* is measured in a calibration experiment by variation of the bath potential without cell. The transconductance  $(\partial I_D / \partial V_{ES})_{V_{DS}}$  is determined at a working point defined by the potentials  $V_E$ ,  $V_D$  and  $V_S$ . When we assume that the transconductance of the calibration experiment is valid for the local recording of a potential, we obtain from the experimental  $\Delta I_D$  the extracellular potential  $V_J$  with  $V_E = 0$  according to (9).

$$\Delta I_D = \left( \frac{\partial I_D}{\partial V_{ES}} \right)_{V_{DS}} V_J \quad (9)$$

We use p-type transistors where all parts of the silicon chip are held at a positive voltage with respect to the bath with  $V_{ES} = V_E - V_S < 0$ ,  $V_{DS} > V_{ES}$ , and with bulk silicon on source potential  $V_B = V_S$ . The bias voltages at the working point prevent cathodic corrosion of the chip and an invasion of sodium ions into the transistors. The thickness of the gate oxide is around 10 nm. In arrays with close spacing, the transistors are placed in a large area with a common gate oxide where they are separated from each other by local field oxide made by a *LOCOS (local oxidation of silicon)* process [14], [15].

**Figure 8:** Intracellular ac stimulation and transistor recording [9], [10].

- (a) Micrograph of leech neuron on *EOSFET* with source S and drain D. The cell is contacted with a patch pipette. From the right a second pipette is impaled to measure the actual voltage  $V_M$  in the cell.
- (b) Amplitude of voltage transfer  $V_J/V_M$  from cell to junction versus frequency  $f$ .
- (c) Phase of the voltage transfer. The dots mark the A-type spectrum, the circles the B-type spectrum.



**Cell stimulation with transistor recording.** We apply an intracellular ac voltage with an amplitude  $V_M(\omega)$  at an angular frequency  $\omega$  to a cell using a patch-pipette in whole cell configuration. The bath is held on ground potential  $V_E = 0$ . We record the complex response  $V_J(\omega)$  in the junction with a transistor [9], [10]. A leech neuron on a transistor is shown in Figure 8a.

Amplitude and phase of the transfer spectrum  $V_J/V_M$  are plotted in Figure 8b and Figure 8c versus the frequency  $f = \omega/2\pi$ . We find two types of spectra: (i) The A-type spectrum has a small amplitude at low frequencies, an increase of the phase around 10 Hz and an increase of the amplitude above 1000 Hz. (ii) The B-type spectrum has a high amplitude at low frequency and a further increase at 1000 Hz. There is only a minor change of the phase around 1000 Hz. Similar measurements can be made with an array of transistors beneath a single leech neuron as illustrated in Figure 9. In that case the voltage transfer as a function of frequency and space coordinate is evaluated with the area contact model [14].

We evaluate the experiment of Fig. 8 with the point-contact model. We insert in (2) an intracellular stimulation  $V_M = V_M \exp(i\omega t)$  with a complex response  $V_J = V_J \exp(i\omega t)$ . When we take into account a leak conductance  $g_{JM}$  in the attached membrane we obtain (10) at  $dV_S/dt = 0$  and  $V_E = 0$  with the time constants  $\tau_J$  and  $\tau_{JM}$  of the junction and the attached membrane.

$$\frac{V_J}{V_M} = \frac{c_M}{c_M + c_S} \cdot \frac{\tau_J/\tau_{JM} + i\omega\tau_J}{1 + i\omega\tau_J}, \quad \tau_J = \frac{c_S + c_M}{g_J + g_{JM}}, \quad \tau_{JM} = \frac{c_M}{g_{JM}}. \quad (10)$$

The high frequency limit of the amplitude  $|V_J/V_M|_\infty = c_M/(c_M + c_S)$  is determined by the capacitances, the low frequency limit  $|V_J/V_M|_0 = g_{JM}/(g_{JM} + g_J)$  by the conductances. There is no phase shift in the limits of low and high frequency. If an intermediate frequency range exists with  $\omega\tau_{JM} \gg 1$  and  $\omega\tau_J \ll 1$ , a phase shift of  $\pi/2$  appears where the current is determined by the membrane capacitance and the junction conductance in series.

We interpret the spectra of Figure 8 in terms of (10) using a membrane capacitance  $c_M = 5 \mu\text{F}/\text{cm}^2$  of leech neurons and a stray capacitance  $c_S = 0.3 \mu\text{F}/\text{cm}^2$  of the chip. In the A-type spectrum the small amplitude at low frequencies indicates a low membrane conductance  $g_{JM}$ . Concomitantly, the increase of the phase at a rather low frequency reflects a large time constant  $\tau_{JM}$  of the membrane. The increase of the amplitude at a high frequency indicates a small time constant  $\tau_J$  and a large conductance  $g_J$ . When we fit the data we obtain  $\tau_{JM} = 14 \text{ ms}$  and  $\tau_J = 25 \mu\text{s}$  and the conductances  $g_{JM} = 0.36 \text{ mS}/\text{cm}^2$  and  $g_J = 217 \text{ mS}/\text{cm}^2$ . In the B-type spectrum, the enhanced amplitude at low frequencies indicates a large membrane conductance  $g_{JM}$ , the further increase at a high frequency is due to a large conductance  $g_J$ . The minor change of phase suggests that a range with  $\omega\tau_{JM} \gg 1$  and  $\omega\tau_J \ll 1$  does not exist, i.e. that the two time constants are similar. When we fit the data we obtain  $\tau_{JM} = 130 \mu\text{s}$  and  $\tau_J = 66 \mu\text{s}$  and the conductances  $g_{JM} = 38.5 \text{ mS}/\text{cm}^2$  and  $g_J = 40.8 \text{ mS}/\text{cm}^2$ .

The crucial difference of A-type and B-type junctions is the leak conductance of the attached membrane [9], [10]. Whereas in an A-type contact the membrane conductance is normal, it is enhanced in B-type junction by two orders of magnitude. From the spe-

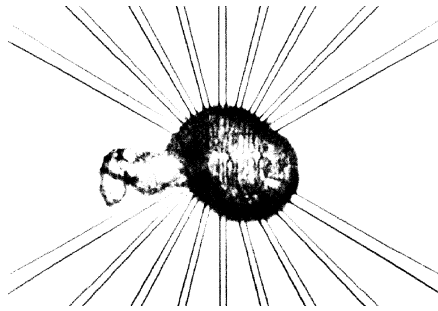


**Figure 9:** Leech neuron on array of field-effect transistors (diameter of the cell about  $60 \mu\text{m}$ ). The array consists of two rows with eight transistors shining through the cell body. The drain contacts are radially directed upwards and downwards. The contact of the common source is at the left and right of the array. The transistors and contacts are separated by local field oxide (*LOCOS* process). The cell is connected with a patch-pipette and the transistor array is used to measure the profile of the extracellular voltage in response to applied intracellular ac voltage [14].

cific junction conductances  $g_j = 217 \text{ mS/cm}^2$  and  $g_j = 40.8 \text{ mS/cm}^2$  we obtain with (3) at  $\theta = 5$  and with an estimated contact area  $A_{JM} = 1000 \mu\text{m}^2$  the sheet resistances  $r_j = 7.7 \text{ M}\Omega$  and  $r_j = 41 \text{ M}\Omega$ . If the cleft is filled with bulk electrolyte ( $\rho_j = 100 \Omega\text{cm}$ ), its width is  $d_j = 130 \text{ nm}$  and  $d_j = 24.4 \text{ nm}$ .

**Bath stimulation with transistor recording.** In a second experiment we apply an extracellular ac stimulation and map the response of the junction with a transistor array [15], [16]. The experiment is performed with a pure lipid membrane [16]. A giant vesicle is sedimented onto the chip and attached by polylysine as shown in Figure 10a.

An ac voltage  $V_E$  is applied to the electrolyte with respect to ground potential and the modulation of the extracellular voltage  $V_J$  with respect to ground is observed in amplitude and phase. The amplitude of voltage transfer  $V_J/V_E$  is plotted in Figure 10b versus the position of the transistors and the frequency  $f$ . At low frequencies, the cleft perfectly follows the voltage in the bath. That coupling is mediated by the conductance of the cleft considering Figure 4a. Already around  $f = 2 \text{ Hz}$  the voltage transfer drops in the center of the junction and a hammock-like profile appears. There the capacitive current through membrane and oxide begins to contribute. At high frequencies where the capacitive current dominates, a plateau is observed again.

We use the area-contact model of (1) to evaluate the profile of the transfer function  $V_J/V_E$  [16]. We do not consider explicitly the current balance of the intracellular space for the area-contact model, but assign the area elements of the free membrane serially to the area elements of the attached membrane. Assuming that the properties of the free and attached membrane are identical, we define an effective area specific capacitance and conductance  $\tilde{c}_M = c_M/(1 + \beta_M)$  and  $\tilde{g}_{JM} = g_{JM}/(1 + \beta_M)$ . This ‘‘local approximation’’ avoids an integration over the attached membrane [13], [16]. The voltage transfer from the electrolyte to the junction in a circular junction with a radius  $a_j$  is given by (11) as a function of the radial coordinate  $a$  and the angular frequency  $\omega$  with the modified Bessel function  $I_0$  and the time constants  $\tau_{JM}$  and  $\tilde{\tau}_{JM}$  and the complex reciprocal length constant  $\tilde{\gamma}_J$  of the core-coat conductor.

$$\frac{V_J(a, \omega)}{V_E(\omega)} = \frac{I_0(\tilde{\gamma}_J a)}{I_0(\tilde{\gamma}_J a_j)} + \frac{i\omega\tau_{JM}}{1 + i\omega\tilde{\tau}_{JM}} \left[ 1 - \frac{I_0(\tilde{\gamma}_J a)}{I_0(\tilde{\gamma}_J a_j)} \right] \quad (11)$$

$$\tau_{JM} = \frac{c_M}{g_{JM}}, \rightarrow \tilde{\tau}_{JM} = \frac{\tilde{c}_M + c_S}{\tilde{g}_{JM}}, \rightarrow \tilde{\gamma}_J^2 = r_j \tilde{g}_{JM} (1 + i\omega\tilde{\tau}_{JM})$$

For a radius  $a_j = 25 \mu\text{m}$  and an area ratio  $\beta_M = 0.7$  estimated from the shape of the vesicle, with the capacitance  $c_M = 0.6 \mu\text{F/cm}^2$  for solventfree lipid bilayers, we obtain a perfect agreement of theory and experiment, when we assume a sheet resistance  $r_j = 130 \text{ G}\Omega$  and a membrane conductance  $g_{JM} < 1 \mu\text{S/cm}^2$ . The low conductance reveals the perfect quality of the lipid bilayer. The sheet resistance is surprisingly high. With  $d_j = 1 \text{ nm}$  measured by *FLIC* microscopy we obtain from  $r_j = \rho_j/d_j$  a specific resistance  $\rho_j = 13000 \Omega\text{cm}$  which is far higher than the specific resistance  $\rho_E = 250 \Omega\text{cm}$  of the bulk electrolyte. The discrepancy can be assigned to a lowered concentration of ions in the narrow cleft, caused by the image force near the oxide and the membrane with their low dielectric constants.

**Chip stimulation with optical recording.** In a third experiment a voltage  $V_S - V_E$  is applied between chip and electrolyte and the response of the voltage  $V_M - V_J$  across the attached membrane is observed with a voltage-sensitive dye [21]. We use cells of the line *HEK 293 (human embryonic kidney cells)* on a chip coated with fibronectin, a protein from the extracellular matrix. The outer surface of the cell membrane is stained with the voltage-sensitive dye *diButyl-Naphthylamine-Butylsulfonato-IsoQuinolinium (BNBIQ)* [19]. At selected wavelengths of excitation and emission, the dye responds with a decrease of fluorescence when a positive voltage is applied to the cytoplasm [18]. Voltage pulses with a height  $V_{SE}^0$  are applied to a highly p-doped silicon chip and the fluorescence change is recorded by signal averaging. A rather thick oxide ( $d_{ox} = 50 \text{ nm}$ ) is chosen to get high fluorescence intensity in front of the reflecting silicon. Optical transients in the attached and free membrane are depicted in Figure 11. After a negative voltage step, the fluorescence transient is negative in the adhesion region indicating a positive change of the membrane voltage  $V_M - V_J$ . For a positive voltage step, the change of the membrane voltage  $V_M - V_J$  is negative. The data are fitted with exponentials. For the attached membrane the time constant is  $2.9 \mu\text{s}$ .

We evaluate the experiment with the point contact model [21]. A step stimulation with an amplitude  $V_{SE}^0$  applied to the chip with respect to the bath is inserted into (2) with  $c_S dV_S/dt = c_S V_{SE}^0 \delta(t)$ . When we neglect all ionic currents we obtain from (4) an

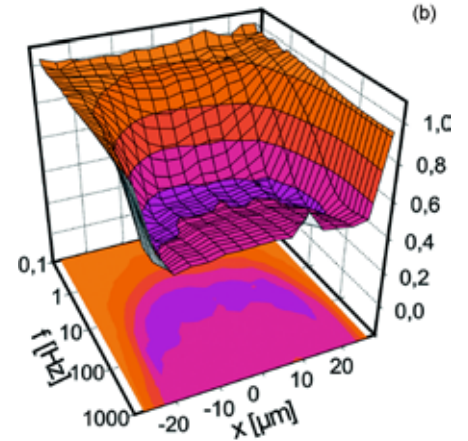
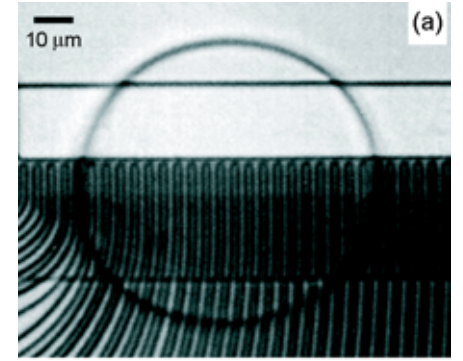


**Figure 10:** Membrane-silicon junction probed by extracellular stimulation and transistor recording [16].

(a) Micrograph of giant lipid vesicle on a linear transistor array. Scale bar  $10 \mu\text{m}$ . The gates are between the ends of the dark lanes of local field oxide.

(b) Amplitude of voltage transfer  $V_J/V_E$  (ratio of voltage amplitude in the cleft and voltage amplitude in the bath with respect to ground) versus position  $x$  and frequency  $f$ .

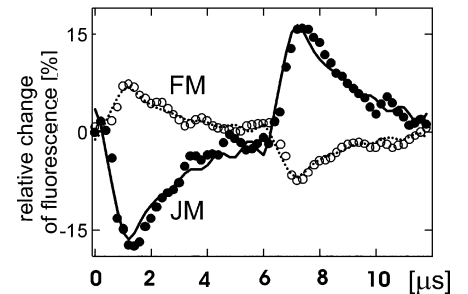


**Figure 11:** Membrane-silicon junction probed with voltage-sensitive dye *BNBIQ* [21]. A negative voltage of  $-6 \text{ V}$  pulse is applied to the chip from  $0 \mu\text{s}$  to  $6 \mu\text{s}$ , a positive pulse of  $+6 \text{ V}$  from  $6 \mu\text{s}$  to  $12 \mu\text{s}$ . The transient change of fluorescence is plotted for the attached (JM) and free membrane (FM) of a *HEK293* cell. The data are fitted with exponentials convoluted with the transfer function of the chip and the response function of the photomultiplier.

exponential response of the voltage across the attached membrane according to (12) with a time constant  $\tilde{\tau}_J$  where the effective capacitance per unit area is  $\tilde{c}_M = c_M/(1 + \beta_M)$

$$\frac{V_M - V_J}{V_{SE}^0} = -\frac{1}{1 + \beta_M} \frac{c_S}{\tilde{c}_M + c_S} \exp\left(-\frac{t}{\tilde{\tau}_J}\right), \quad \tilde{\tau}_J = \frac{\tilde{c}_M + c_S}{g_J} \quad (12)$$

From the experimental time constant  $\tilde{\tau}_J = 2.9 \mu\text{s}$  with  $c_M = 1 \mu\text{F}/\text{cm}^2$ ,  $c_S = 0.07 \mu\text{F}/\text{cm}^2$  and  $\beta_M = 0.4$  we obtain a specific conductance  $g_J = 270 \text{ mS}/\text{cm}^2$  of the junction. Using (3) with  $\theta = 5$  and a contact area  $A_{JM} = 725 \mu\text{m}^2$ , a sheet resistance of  $r_J = 8 \text{ M}\Omega$  is evaluated. That result is similar to the A-type junction of leech neuron. For the *HEK293* cells, however, we are able to measure the width of the cleft by *FLIC* microscopy. We find  $d_J = 50 \text{ nm}$ . From  $r_J = \rho_J/d_J$  we obtain a specific resistance  $\rho_J = 40 \Omega\text{cm}$  in the cleft. This value is quite similar to the surrounding bath with a specific resistance  $74 \Omega\text{cm}$ . We conclude: the cleft between a cell and a silicon chip is filled with bulk electrolyte. Whether the difference of  $40 \Omega\text{cm}$  and  $74 \Omega\text{cm}$  is significant has to be checked by more detailed experiments.

**Conclusion.** The cleft between neuronal cells and chips has an electrical resistance that corresponds to a thin film of bulk electrolyte. The sheet resistance is in the order of  $r_J \approx 10 \text{ M}\Omega$  with a global resistance around  $G_J^{-1} \approx 1 \text{ M}\Omega$ . There is no gigaohm seal between neuronal cells cultured on a chip. It should be noted that the width of the cleft is far larger than the thickness of the diffuse electrical double layer at the silicon dioxide and at the membrane with a Debye length around  $\kappa_D^{-1} \approx 1 \text{ nm}$  in  $100 \text{ mM NaCl}$  and also far larger than the Bjerrum length  $l_B \approx 0.7 \text{ nm}$  of Coulombic interactions which governs the interaction with image charges in membrane and silicon dioxide. It will be a difficult task to enhance the sheet resistance by lowering the width or by enhancing the specific resistance of the cleft.

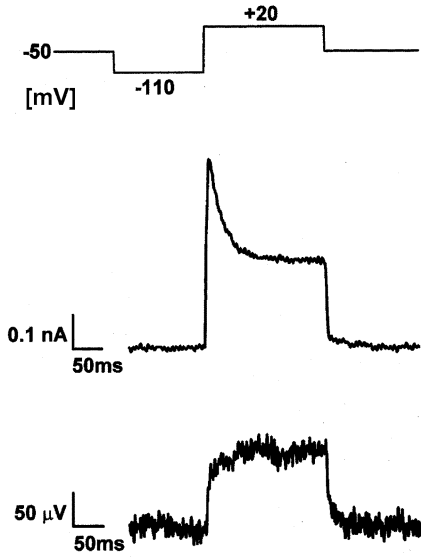


**Figure 12:** Rat neuron on a transistor under voltage-clamp [22]. The protocol of the intracellular voltage  $V_M$  is shown at the top. In the center the total membrane current  $I_M$  is plotted, at the bottom the extracellular voltage  $V_J$  recorded by a transistor obtained by averaging 30 records.

## 2.4 Ion Channels in Cell-Silicon Junction

During neuronal excitation, the *Transductive Extracellular Potential*  $V_J(t)$  depends on the current through ion conductances in the attached membrane. During capacitive stimulation of neurons the primary target of the *Transductive Extracellular Potential*  $V_J(t)$  are the ion conductances in the attached membrane. Thus we have to ask: (i) Are there functional ion channels in the contact region at all? (ii) Is the density of ion channels in the contact the same as in the free membrane? We consider two systems, intrinsic potassium channels in rat neurons and recombinant potassium channels in *HEK293* cells.

**Rat neurons.** Neurons from rat hippocampus are cultured on a chip with transistors as shown in Figure 2. The intracellular voltage of a cell is varied by the whole-cell patch-clamp technique. Simultaneously, we measure the current  $I_M$  through the total membrane with the micropipette and the extracellular voltage in the contact area  $V_J$  with a transistor, holding the bath at ground potential [22]. The sodium current is inhibited by tetrodotoxin. The intracellular voltage  $V_M$ , the outward current  $I_M$  and transistor record  $V_J$  are plotted in Figure 12.

At a depolarization  $V_M = 20 \text{ mV}$  there is a stationary current  $I_M = 0.25 \text{ nA}$  and a superposed transient current. These two current components are due to two different potassium conductances, a K-type conductance and an inactivating A-type conductance. The extracellular voltage  $V_J$  detected by the transistor shows a stationary response that matches the stationary K-type current, but no component corresponding to the A-type current [22]. The slow relaxation of the transistor signal after the depolarizing and hyperpolarizing step is due to electrodiffusion effects.

We discuss the result in terms of the point-contact model using (2) and (4) [22], [23]. At a constant voltage  $V_M$ , the membrane current  $I_M$  for a single ion conductance with an average area specific conductance  $g_M^i$  in the whole cell membrane is given by (13) with the total membrane area  $A_M$ , assuming that the extracellular voltage is small with  $V_J \ll V_M - V_0^i$ . The extracellular voltage  $V_J$  is described by (14) with the specific conductance  $g_{JM}^i$  in the attached membrane.

$$I_M = A_M g_M^i (V_M - V_0^i) \quad (13)$$

$$V_J = \frac{1}{g_J} g_{JM}^i (V_M - V_0^i) \quad (14)$$

If the channels in the attached and free membrane have the same functionality, the relative conductances  $g_M^i/\bar{g}_M^i$  and  $g_{JM}^i/\bar{g}_{JM}^i$  follow the same voltage-dependence where  $\bar{g}_M^i$  and  $\bar{g}_{JM}^i$  are the maximum conductances with open channels. Considering (13) and (14), the transistor record  $V_J$  and the pipette record  $I_M$  are proportional to each other for all voltages  $V_M$  according to (15).

$$\frac{V_J}{I_M} = \frac{1}{g_J A_M} \frac{\bar{g}_{JM}^i}{\bar{g}_M^i} \quad (15)$$

Considering Figure 12 with (15) we conclude: (i) The absence of a transient in the transistor response indicates that there is no A-type potassium conductance in the attached membrane with  $\bar{g}_{JM}^A \ll \bar{g}_M^A$ . (ii) The visible response of the transistor shows that functional K-type channels exist in the junction. To evaluate the ratio  $\bar{g}_{JM}^K/\bar{g}_M^K$  from the experimental  $V_J/I_M = 480 \text{ k}\Omega$  with (15) we need a value of the scaling factor  $(g_J A_M)^{-1}$ .

$g_J$  and  $A_M$  are obtained by an ac measurement when the channels are closed. From (2) and (4) we obtain for the complex response of the current  $I_M$  and of the extracellular voltage  $V_J$  (16) and (17) at  $g_{JM}^i = 0$  and  $\omega\tau_J \ll 1$ . The scaling factor is given by the ratio  $V_J/I_M$  according to (18).

$$I_M = i\omega c_M A_M V_M \quad (16)$$

$$V_J = \frac{i\omega c_M}{g_J} V_M \quad (17)$$

$$\frac{V_J}{I_M} = \frac{1}{g_J A_M} \quad (18)$$

From the response by ac stimulation at  $\omega = 200 \text{ Hz}$ , we obtain with (16) and (17) a membrane area  $A_M = 1100 \mu\text{m}^2$  and a junction conductance  $g_J = 1000 \text{ mS/cm}^2$  at  $c_M = 1 \mu\text{F/cm}^2$ . With the resulting scaling factor  $(g_J A_M)^{-1} = 91 \text{ k}\Omega$  and with  $V_J/I_M = 480 \text{ k}\Omega$  the ratio of the maximum conductances in the attached and total membrane is  $\bar{g}_{JM}^K/\bar{g}_M^K = 5.3$  using (15). We conclude: the K-type potassium channels are significantly accumulated in the junction.

**Recombinant channels.** A more detailed investigation is possible with recombinant *hSlo* potassium channels that are overexpressed in *HEK293* cells. No signal averaging is required, and the voltage-dependent gating can be analyzed in detail. The cells are cultured on a transistor array as depicted in Figure 13a.

The voltage  $V_M$  in the cell is changed step by step with a patch-pipette, and the total membrane current  $I_M$  and the extracellular voltage  $V_J$  are simultaneously recorded [23]. Examples are shown in Figure 13b for a high extracellular potassium concentration. A depolarization leads to an enhancement of the current and a correlated enhancement of the transistor signal. Thus, functional *hSlo* potassium channels must exist in the junction. (With low extracellular potassium concentrations, slow transients appear in the transistor signal that are due to electrodiffusion effects.)

In that experiment we are able to check whether the functionality of the channels in the attached and free membrane is the same [23]. We plot  $V_J$  versus  $I_M$  in Figure 13c for all voltages  $V_M$  and obtain a strict linear relation over the whole range of gating. The result shows that (15) is valid with a constant ratio  $V_J/I_M = 73 \text{ k}\Omega$ . We measure the scaling factor  $(g_J A_M)^{-1}$  with an ac stimulation at  $\omega = 6 - 20 \text{ Hz}$ . From the current and the transistor signal we obtain with (16) and (17) a membrane area  $A_M = 2360 \mu\text{m}^2$  and a junction conductance  $g_J = 1960 \text{ mS/cm}^2$  at  $c_M = 1 \mu\text{F/cm}^2$ . The high junction conductance indicates a small effective radius  $a_j$  of the junction (3). It is due to a peripheral location of the transistor in the area of cell adhesion. With the scaling factor  $(g_J A_M)^{-1} = 22 \text{ k}\Omega$  and with  $V_J/I_M = 73 \text{ k}\Omega$ , the ratio of the maximum area specific conductance in the attached and total membrane is  $\bar{g}_{JM}^{\text{Slo}}/\bar{g}_M^{\text{Slo}} = 3.3$  using (15). Thus the recombinant *hSlo* potassium channels are accumulated in the attached membrane.

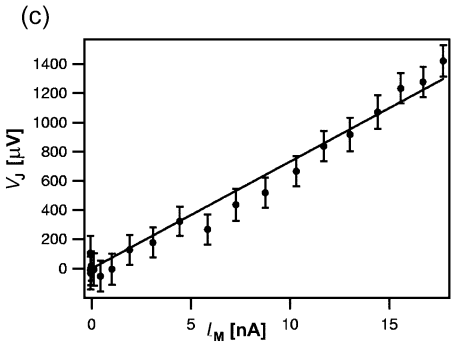
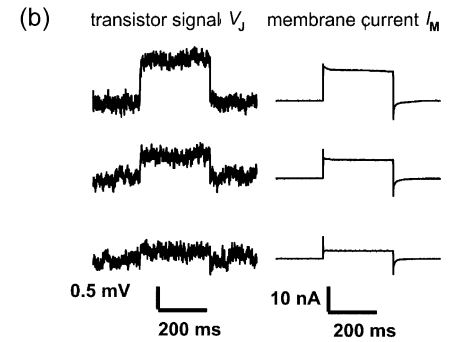
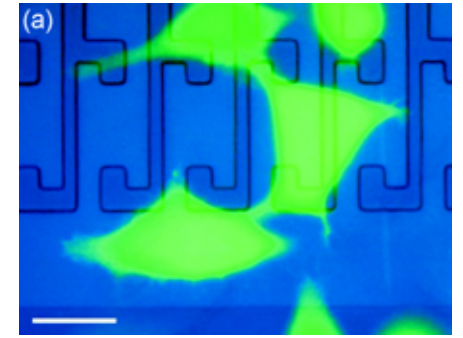


**Figure 13:** Recombinant *hSlo* potassium channels on a transistor [23].

(a) *HEK293* cells on linear transistor array. With a blue illumination the transfected cells appear in the color of the fluorescence of GFP (green fluorescent protein) used as a marker.

(b) Iono-electronic coupling at three intracellular voltages  $V_M = 30, 45, 58 \text{ mV}$ . Left: extracellular voltage  $V_J$  in the cell-silicon junction. Right: current  $I_M$  through the total cell membrane. Intracellular potassium concentration  $152 \text{ mM}$ , extracellular potassium concentration  $100 \text{ mM}$ .

(c) Extracellular voltage  $V_J$  versus membrane current  $I_M$ . The regression line has a slope  $V_J/I_M = 73 \text{ k}\Omega$ .

**Sensorics.** An overexpression of ligand-gated channels and transistor recording is a promising approach to develop cell-based biosensors. In such systems the intracellular voltage is not controlled. The *TEP* is obtained by combining (2), (3) and (4) for small signals with  $V_J \ll V_M - V_0^i$  and  $dV_J \ll dV_M$  at  $V_E = 0$  according to (19): A cellular electronic sensor relies on an accumulation or depletion of channels with  $g_{JM}^i - g_{FM}^i \neq 0$ , a high driving voltage  $V_M - V_0^i$  and a junction with a large radius  $a_J$ , a high specific resistance  $\rho_J$  and a small distance  $d_J$ .

$$V_J = \frac{\rho_J a_J^2}{5d_J(1 + \beta_M)} (g_{JM}^i - g_{FM}^i) (V_M - V_0^i) \quad (19)$$

**Conclusion.** The combination of transistor recording with whole-cell patch-clamp shows that functional ion channels exist in the area of cell adhesion. Important for neuronal interfacing and cellular biosensorics is the observation, that ion channels are selectively accumulated and depleted. A control of the expression and sorting of ion channels is an important task to optimize cell-chip contacts.

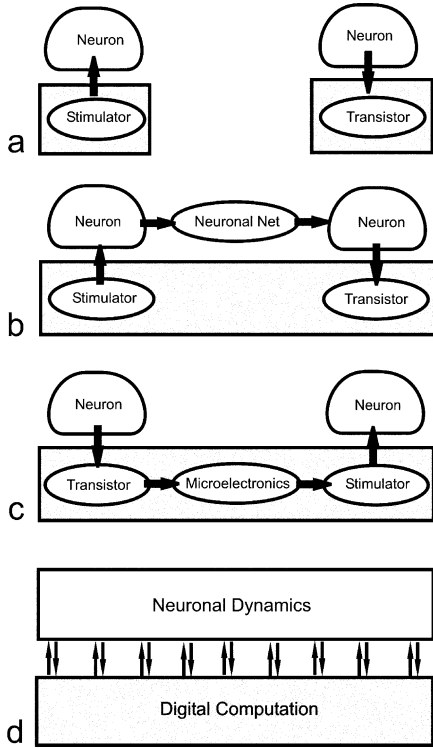


**Figure 14:** Neuroelectronic hybrids.

- (a) Capacitive stimulation and transistor recording of individual neurons from semiconductor.  
 (b) Two-neuron pathway with capacitive stimulation, signal transmission through neuronal network and transistor recording at a second neuron.  
 (c) Two-neuron pathway with transistor recording, signal processing by microelectronics on the chip and capacitive stimulation of a second neuron.  
 (d) Integration of neuronal dynamics and digital electronics by bidirectional signaling on a microscopical level.

### 3 Neuron-Silicon Circuits

Cell-silicon junctions are the basis for an integration of neuronal dynamics and digital electronics. The first step is an interfacing of individual nerve cells and silicon microstructures (Figure 14a) with (i) eliciting neuronal activity by capacitive stimulation from the chip and (ii) recording of neuronal activity by a transistor. On a next level, pairs of nerve cells are coupled to a chip with two fundamental pathways: (i) Stimulation of a neuron, signal transfer through a neuronal network with synapses to a second neuron and recording of neuronal activity there by a transistor (Figure 14b). (ii) Recording activity of one neuron by a transistor, signal transfer through the microelectronics of the chip and capacitive stimulation of a second neuron (Figure 14c). In a further step, defined neuronal networks are created on the chip such that an intimate communication of network dynamics and computation can be envisaged (Figure 14d).

Identified neurons from invertebrates are preferred in these experiments because they are large and easy to handle, because they form strong neuroelectronic junctions, and last but not least, because small neuronal networks have a distinct biological function in invertebrates and may be reconstituted and studied on a chip.

#### 3.1 Transistor Recording of Neuronal Activity

The activity of a nerve cell – an action potential – consists in a fast opening of sodium channels with a concomitant current into the cell and a delayed opening of potassium channels with a compensating outward current. The ionic currents are coupled by the membrane potential  $V_M(t)$  which controls the opening and closing of the channels. The voltage transient  $V_M(t)$  is confined by the reversal voltages of sodium and potassium channels. The neuronal excitation drives ionic and capacitive current through the membrane attached to a chip. That current is squeezed through the cleft between cell and chip and gives rise to a *Transductive Extracellular Potential*  $V_J(t)$  that is recorded by a transistor. First we derive  $V_J(t)$  expected for neuronal excitation using the point-contact model. Then we consider transistor recordings of leech and rat neurons.

**Small signal approximation.** The *Transductive Extracellular Potential* is determined by the coupled dynamics of the extracellular and intracellular potentials  $V_M$  and  $V_J$  according to (2) and (4). We assume that the extracellular potential is small with  $V_J \ll V_M - V_0^i$  and  $dV_J \ll dV_M$ , and that the capacitive current to the chip is negligible. With  $V_E = 0$  we obtain (20) and (21) with the current  $j_{INJ}$  injected by a pipette per unit area of the cell membrane [24]: The extracellular potential  $V_J(t)$  is determined by the capacitive and ionic current through the attached membrane. The intracellular potential  $V_M(t)$  is governed by the currents through attached and free membrane.

$$g_J V_J = \sum_i g_{JM}^i (V_M - V_0^i) + c_M \frac{dV_M}{dt} \quad (20)$$

$$(1 + \beta_M) c_M \frac{dV_M}{dt} = - \sum_i (g_{FM}^i + \beta_M g_{JM}^i) (V_M - V_0^i) + (1 + \beta_M) j_{INJ} \quad (21)$$

**A-, B- and C-type response.** When the attached membrane contains no voltage-gated conductances, we obtain (22) with a leak conductance  $g_{JM}$  in the attached membrane using (20).

$$g_J V_J = g_{JM} V_M + c_M \frac{dV_M}{dt} \quad (22)$$

For negligible leak conductance, the capacitive current through the attached membrane dominates. Then the *TEP* is proportional to the first derivative of the intracellular voltage with  $V_J \propto dV_M/dt$  [2]. This situation corresponds to the A-type junction observed in ac measurements. We call it an A-type response. For a dominating ohmic leak conductance, the *TEP* reflects the intracellular waveform itself with  $V_J \propto V_M$  [9], [10], [25]. We call it a B-type response in analogy to the B-type junction found with ac experiments.

When we insert (21) into (20), the capacitive current is expressed by the ionic current through the free membrane and we obtain (23). The *Transductive Extracellular Potential* is determined by the differences  $g_{JM}^i - g_{FM}^i$  of the area specific ion conductances in the attached and free membrane [24].

$$g_J V_J = \frac{1}{1 + \beta_M} \sum_i (g_{JM}^i - g_{FM}^i) (V_M - V_0^i) + j_{INJ} \quad (23)$$

This striking relation shows that the *TEP* of an action potential relies on an inhomogeneity of the membrane. In particular (23) reveals, that a selective accumulation or depletion of voltage-gated channels can give rise to a wide spectrum of waveforms  $V_J(t)$ . We call them C-type responses [26]. Details must be treated by numerical simulation. A special signal is expected when all conductances are accumulated by the same accumulation factor  $\mu_j^i = g_{JM}^i / g_{FM}^i$ . For  $\mu_j > 1$  the response is proportional to the negative first derivative of the intracellular voltage according to (24).

$$V_J = \frac{1 - \mu_j}{1 + \mu_j \beta_M} \frac{c_M}{g_J} \frac{dV_M}{dt} \quad (24)$$

**Leech neuron.** Transistor records of leech neurons are shown in Figure 15. Two positions of the cells are illustrated in Figure 15a and Figure 15b, with the cell body right on a transistor [25] and with the axon stump placed on a transistor array [26]. The cells are impaled with a micropipette and action potentials are elicited by current injection. The intracellular potential  $V_M(t)$  is measured with the pipette. The response of the transistors is calibrated in terms of the extracellular potential  $V_J(t)$  on the gate. Three types of records are depicted in Figure 15c: (i) With a cell body on a transistor,  $V_J(t)$  resembles the first derivative of the intracellular voltage  $V_M(t)$ . (ii) With a cell body on a transistor,  $V_J(t)$  resembles the intracellular voltage  $V_M(t)$  itself. (iii) With an axon stump on a transistor,  $V_J(t)$  resembles the inverted first derivative of  $V_M(t)$ .

The results perfectly match the A-type, the B-type and the special C-type response considered above. The C-type record is observed only when the axon stump is placed on the transistor (Figure 15b). That region is known for its enhanced density of ion channels. The small amplitude is due to the small size of the axon stump with a high junction conductance  $g_J$  according to (3). The density of channels is depleted in the cell body where we observe A-type and B-type records.

**Rat neuron.** Neurons from rat hippocampus are cultured for seven days in neurobasal medium on a chip coated with polylysine [27], [29]. Selected cells, such as depicted in Figure 2, are contacted with a patch pipette and action potentials are elicited by current pulses. Transistor records are obtained by signal averaging, locking the transistor signal to the maximum of the intracellular transient. A result obtained with 63 sweeps is shown in Figure 16.

The amplitude of the extracellular potential  $V_J(t)$  is around 0.15 mV. The action potential  $V_M(t)$  give rise to two positive transients in  $V_J(t)$ , one in the rising phase and one in the falling phase. The upward and downward jumps in the record match the upward and downward steps of the injection current (23). The small amplitude of the transistor record is a consequence of a high junction conductance  $g_J$  which is expected for the small size of rat neurons (3). From an ac measurement we estimate  $g_J = 600 - 700 \text{ mS/cm}^2$ . The shape of the transistor response can be interpreted in terms of (23): (i)

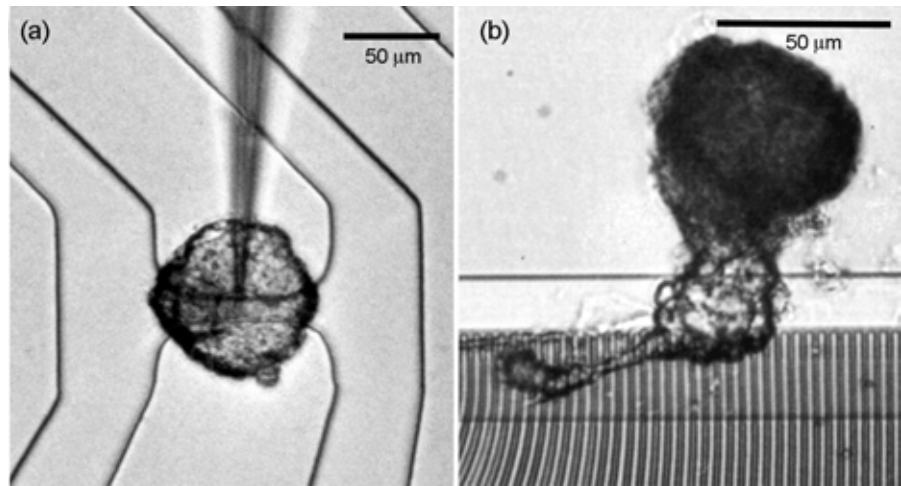
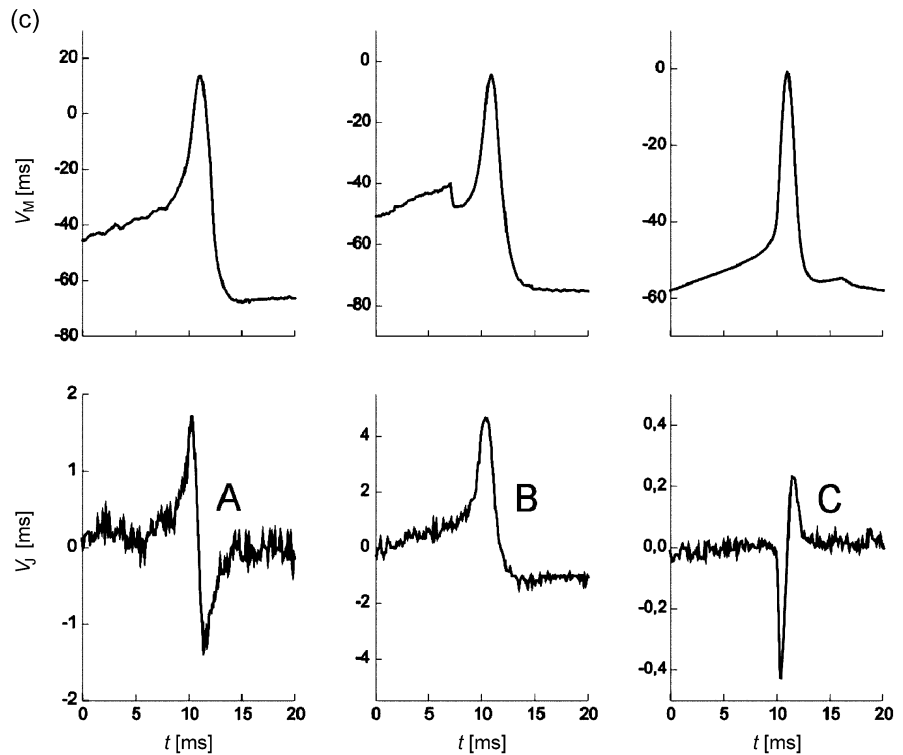


**Figure 15:** Transistor recording of neuronal excitation in leech neurons [25], [26].

(a) Cell body of a neuron on the open gate oxide of a field-effect transistor. Scale bar 50  $\mu\text{m}$ . The cell is impaled with a micropipette.

(b) Axon stump of a neuron on a linear array of field-effect transistors. Scale bar 50  $\mu\text{m}$ .

(c) A, B and C-type coupling. The upper row shows the intracellular voltage  $V_M(t)$ , the lower row the extracellular voltage  $V_J(t)$  on the gate oxide. A and B-type couplings are observed for arrangement a), C-type couplings for arrangement b).



The positive peak in the rising phase is related with the sodium current. Considering (23) with  $V_M - V_0^{\text{Na}} < 0$ , it must be connected with  $g_{\text{JM}}^{\text{Na}} - g_{\text{FM}}^{\text{Na}} < 0$ , i.e. a depletion of sodium channels in the junction. In other words, the sodium inward current through the free membrane gives rise to a capacitive outward current through the attached membrane. (ii) The positive peak in the falling phase can be assigned to a potassium outward current through the attached membrane, considering an accumulation of potassium channels with  $g_{\text{JM}}^{\text{K}} - g_{\text{FM}}^{\text{K}} > 0$  and  $V_M - V_0^{\text{K}} > 0$ .

**Conclusion.** Neuronal activity is detected by field-effect transistors. The response is rationalized by a *Transductive Extracellular Potential* in the cell-chip contact that plays the role of a gate voltage. There is no unique response to action potentials, the shape of the extracellular record depends on the cell type and the cell area attached to the chip. The amplitude of the extracellular records is small, because the junction conductance is high compared to the effective ion conductances in the contact with  $g_J \gg g_{\text{JM}}^i - g_{\text{FM}}^i$ . The signals are particularly weak for mammalian neurons due to their small size. We may attempt to optimize recording (i) by improving the cell-chip contact - reducing the width of the cleft or enhancing its specific resistance, (ii) by enhancing the inhomogeneity of channel distribution using recombinant methods or (iii) by lowering the noise of the transistors choosing improved design and fabrication.

### 3.2 Capacitive Stimulation of Neuronal Activity

A changing voltage  $V_S(t)$  applied to a stimulation spot beneath a neuron leads to a capacitive current through the insulating oxide. The concomitant current along the cleft between cell and chip gives rise to a *Transductive Extracellular Potential*  $V_J(t)$  beneath the neuron. As a result voltage-gated ion channels may open in the membrane and an action potential  $V_M(t)$  may arise. We consider first the extracellular and intracellular voltage of the point-contact model after stimulation with a voltage step. Then we discuss experiments with a voltage step and with a burst of voltage pulses.

**A-type stimulation.** Stimulation starts from the resting state of a neuron with low ion conductances. For the initial phase, we completely neglect the ion conductances in the attached and free membrane. Considering the coupling of the intracellular and extracellular potentials  $V_M(t)$  and  $V_J(t)$  with (2) and (4), we obtain (25) and (26) for  $V_E = 0$  with  $\tilde{c}_M = c_M/(1 + \beta_M)$  [3], [21].

$$(c_S + \tilde{c}_M) \frac{dV_J}{dt} + g_J V_J = c_S \frac{dV_S}{dt} \quad (25)$$

$$\frac{dV_M}{dt} = \frac{\beta_M}{1 + \beta_M} \frac{dV_J}{dt} \quad (26)$$

For a voltage step of height  $V_S^0$  at time  $t=0$  the perturbation of the junction is  $c_S dV_S/dt = c_S V_S^0 \delta(t)$ . The voltages across the attached and free membrane  $V_M - V_J$  and  $V_M$  respond with exponentials for  $t > 0$  according to (27) with the time constant  $\tilde{\tau}_J$ .

$$\begin{aligned} V_M - V_J &= - \frac{1}{1 + \beta_M} \frac{c_S}{\tilde{c}_M + c_S} V_S^0 \exp\left(-\frac{t}{\tilde{\tau}_J}\right) \\ V_M &= \frac{\beta_M}{1 + \beta_M} \frac{c_S}{\tilde{c}_M + c_S} V_S^0 \exp\left(-\frac{t}{\tilde{\tau}_J}\right) \end{aligned} \quad \tilde{\tau}_J = \frac{c_S + \tilde{c}_M}{g_J} \quad (27)$$

For a positive voltage step  $V_S^0 > 0$ , the voltage drop is negative (hyperpolarizing) across the attached membrane and positive (depolarizing) across the free membrane. For  $V_S^0 = 5\text{V}$ ,  $c_S = 0.35 \mu\text{F}/\text{cm}^2$ ,  $c_M = 5 \mu\text{F}/\text{cm}^2$  and  $\beta_M = 1/6$  as estimated for leech neurons, the voltage amplitude is  $|V_M - V_J|_0 \approx 300 \text{mV}$  across the attached membrane and  $|V_M|_0 \approx 50 \text{mV}$  across the free membrane. With  $g_J \approx 200 \text{mS}/\text{cm}^2$  of an A-type junction of a leech neuron, we expect a time constant  $\tilde{\tau}_J \approx 25 \mu\text{s}$ . For mammalian neurons, the time constants are even shorter due to the larger  $g_J$  and smaller  $c_M$  as verified by optical recording (Figure 11). The crucial question is, how such short transients can affect the ion conductance of a membrane.

**B-type stimulation.** We consider the role of a leak conductance  $g_{JM}$  in the attached membrane. To avoid complicated equations, we assume that the intracellular voltage is small compared to the extracellular voltage with  $V_M \ll V_J$  and  $dV_M \ll dV_J$ . From (2) we obtain (28) for the extracellular voltage at  $V_E = 0$  with the exponential solution of (29) after a voltage step of height  $V_S^0$ .

$$(c_S + c_M) \frac{dV_J}{dt} + (g_{JM} + g_J) V_J = c_S \frac{dV_S}{dt} \quad (28)$$

$$V_J = \frac{c_S}{c_M + c_S} V_S^0 \exp\left(-\frac{t}{\tau_J}\right), \quad \rightarrow \quad \tau_J = \frac{c_M + c_S}{g_{JM} + g_J} \quad (29)$$

The upward jump of the extracellular transient  $V_J(t)$  injects a charge pulse into the cell by capacitive polarization. That charge is withdrawn during the decaying exponential. Additional charge is injected during the exponential transient through a leak conductance in the attached membrane. Using (2) we obtain the injected current per unit area according to (30).

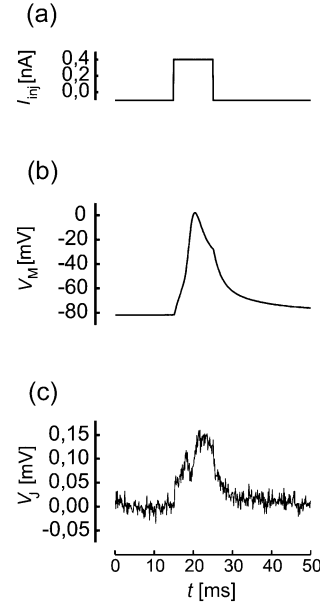


**Figure 16:** Transistor record of neuronal excitation in a rat neuron [29].  
 (a) Injection current applied by a patch pipette.  
 (b) Intracellular potential  $V_M(t)$ .  
 (c) Transistor record scaled as an extracellular potential  $V_J(t)$  on the gate (63 averaged signals).

$$j_{JM} = V_S^0 c_S \left\{ \frac{c_M}{c_M + c_S} \left[ \delta(t) - \frac{\exp(-t/\tau_J)}{\tau_J} \right] + \frac{g_{JM}}{g_J + g_{JM}} \frac{\exp(-t/\tau_J)}{\tau_J} \right\} \quad (30)$$

Considering (2), the perturbation of the intracellular potential  $V_M(t)$  is obtained from (31).

$$c_M \frac{dV_M}{dt} + \sum_i g_{FM}^i (V_M - V_0^i) = \beta_M j_{JM} \quad (31)$$

When we neglect the voltage-gated conductances  $g_{FM}^i$  in the free membrane in the stimulation phase, the intracellular potential  $V_M(t)$  is given by (32) with the resting potential  $V_M^0$ .

$$V_M = V_M^0 + V_S^0 \beta_M \frac{c_S}{c_M} \left[ \left( \frac{c_M}{c_M + c_S} - \frac{g_{JM}}{g_{JM} + g_J} \right) \exp\left(-\frac{t}{\tau_J}\right) + \frac{g_{JM}}{g_{JM} + g_J} \right] \quad (32)$$

There is a jump of the intracellular voltage at  $t=0$  due to the capacitive effect. The subsequent relaxation within the time  $\tau_J$  levels out at a potential determined by the leak conductance. There is a stationary change of the intracellular potential (33)

$$V_M - V_M^0 = V_S^0 \beta_M \frac{c_S}{c_M} \frac{g_{JM}}{g_{JM} + g_J} . \quad (33)$$

If that potential change is above a threshold, an action potential is elicited, if it is below the threshold, it relaxes with the time constant of the total cell. For a positive voltage step  $V_S^0 = 5V$  applied to the B-type junction of a leech neuron with  $\beta_M = 1/6$ ,  $c_S = 0.35 \mu F/cm^2$ ,  $c_M = 5 \mu F/cm^2$ ,  $g_{JM} \approx 40 \text{ mS/cm}^2$  and  $g_J \approx 40 \text{ mS/cm}^2$  we expect a depolarization of  $V_M - V_M^0 = 25 \text{ mV}$ .

**C-type stimulation.** When we take into account voltage-gated conductances in the attached and free membrane, different neuronal responses are expected to a positive or negative voltage step, depending on channel sorting. Such junctions must be treated by numerical simulation on the basis of an assumed dynamics of voltage-gated channels [28].

**Step stimulation of leech neuron.** Neurons from the leech are stimulated by a single positive voltage step applied to a capacitive stimulation spot on a silicon chip as illustrated in Figure 17a [3]. The height of the steps is  $V_S^0 = 4.8, 4.9, 5.0 \text{ V}$ . The intracellular response  $V_M(t)$  is shown in Figure 17b. When the height exceeds a threshold, an action potential is elicited.

A positive step in an A-type contact leads to a hyperpolarizing effect on the attached membrane. No sodium channels can open there to induce an action potential. The free membrane is affected by a depolarizing transient with a small amplitude  $|V_M| \approx 50 \text{ mV}$  and a time constant  $\tau_J \approx 25 \mu s$ . It is difficult to imagine, how sodium channels with a time constant in the millisecond range are able to respond to such short transients. Thus it is likely that a B-type junction exists. The *Transductive Extracellular Potential*  $V_J(t)$  injects Ohmic current into the cell through a leak conductance  $g_{JM}$  according to (30). A resulting quasi-stationary depolarization of about 25 mV is sufficient to elicit an action potential.

**Burst stimulation of snail neuron.** In many junctions of neurons from leech and snail, excitation is achieved only when a burst of voltage pulses is applied to a chip [30], [34], [35]. An example is shown in Figure 18. A snail neuron is attached to a two-way junction made of a stimulation area and a transistor (Figure 18a). When a burst of voltage pulses is applied to the stimulation area, the intracellular voltage  $V_M(t)$  responds with short capacitive transients at the rising and falling edge of each pulse and a stationary depolarization during the pulses as illustrated in Figure 18b. After the third pulse, the intracellular potential rises such that an action potential is elicited [34]. The transistor allows us a look into the junction. The rising and falling edges of each pulse lead to capacitive transients  $V_J(t)$ . At the rising edge an additional negative transient  $V_J(t)$  is initiated that slowly decays during the pulse and during the subsequent pulse interval.

We conclude that the positive capacitive transients in the cleft at the onset of the pulses induce an ionic inward current through the attached membrane. That conductance decays slowly and is not affected by the negative capacitive transient. It is responsible for the intracellular depolarization  $V_M(t)$ . However, the positive extracellular transients

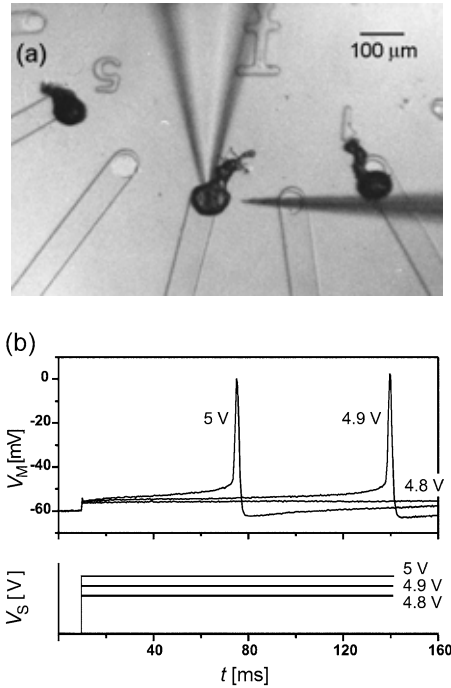


**Figure 17:** Capacitive stimulation by silicon chip [3].

(a) Leech neurons are attached to circular stimulation spots (from 20  $\mu m$  to 50  $\mu m$  diameter) covered by 10 nm silicon dioxide. The rest of the chip is insulated by a 1  $\mu m$  thick field oxide. One neuron is impaled with a micropipette electrode. An additional electrode (right) measures the local bath potential. Scale bar 100  $\mu m$ .

(b) Top: intracellular voltages  $V_M(t)$ . Bottom: voltage steps  $V_S(t)$  applied to the chip (not on scale).

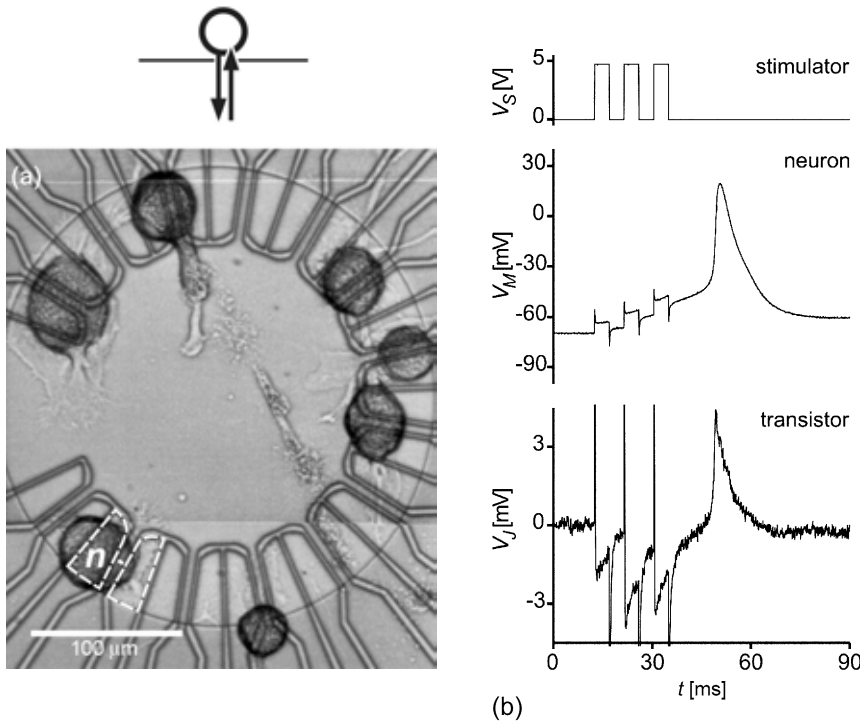


**Figure 18:** Capacitive stimulation of neuron by a burst of voltage pulses [34].

(a) Micrograph of snail neurons on a chip with a circular arrangement of two-way contacts. The stimulation area with two wings under neuron  $n$  is marked with a dashed line, the transistor is located between the two wings. Scale bar 100  $\mu\text{m}$ .

(b) Voltage  $V_S(t)$  applied to the stimulation area. (c) Intracellular voltage  $V_M(t)$  measured with an impaled pipette.

(d) Extracellular voltage  $V_J(t)$  measured with the transistor.

has a hyperpolarizing effect on the attached membrane and cannot open voltage-gated channels there. Maybe the stimulus with an amplitude  $|V_M - V_{J0}| \approx 300$  mV is sufficient to induce a transient electroporation of the membrane. The resulting inward current is recorded by the transistor and depolarizes the cell. Possibly the negative capacitive transient is not sufficient to induce electroporation, because its electrical field is opposite to the given electrical field in the resting state.

**Conclusion.** The concept of a core-coat conductor can guide a rationalization of capacitive stimulation of neuronal activity on silicon chips. But the situation is less clear than with transistor recording. Optical recording directly reveals that fast voltage transients actually exist in the attached and free membrane. But how those transients affect the cell is uncertain. Current injection through a leaky membrane, capacitive gating of ion channels and transient electroporation are difficult to distinguish. Further studies on neuronal excitation are required with a recording of the local voltage by transistors or voltage-sensitive dyes, comparing voltage-clamp and current-clamp. Detailed studies on the capacitive gating of ion channels and on electroporation will be most helpful. An optimized stimulation may be achieved (i) by lowering the junction conductance, (ii) by inserting recombinant ion channels into the junction and (iii) by fabricating stimulation spots with an enhanced specific capacitance.

### 3.3 Circuits with Two Neurons on Silicon Chip

We consider two hybrid circuits with two neurons on a silicon chip, the signal transmission from a neuron through a chip to another neuron and the signal transmission from the chip through two synaptically connected neurons back to the chip (Figure 14). With respect to the second device, the formation of electrical synapses and the immobilization of neurons are addressed.

**Neuron-chip-neuron.** The equivalent circuit of recording and stimulation of two neurons on a chip is shown in Figure 19: A field-effect transistor probes the extracellular voltage  $V_J$  in the junction between the first cell and the chip as caused by the membrane currents of an action potential. Capacitive stimulation induces a voltage  $V_J$  in the junction of the second cell to elicit neuronal excitation by activating membrane conductances. The processing unit accomplishes five tasks (Figure 19): (i) The source-drain current of the transistor is transformed to a voltage and amplified. (ii) The response to an individual action potential is identified by a threshold device (Schmitt trigger). (iii) A

**Figure 19:** Electronic coupling of two disconnected neurons [31], [32]. In the upper part the interfacing between the neurons and the semiconductor is represented as an equivalent circuit with the point-contact model. In the lower part the function of the interneuron unit is sketched as a block circuit with three stages: (i) amplification and signal recognition, (ii) delay line and (iii) pulse generator. The cross talk from stimulation to recording is marked by a dashed line, the reset of the flip-flop after stimulation by a drawn line.

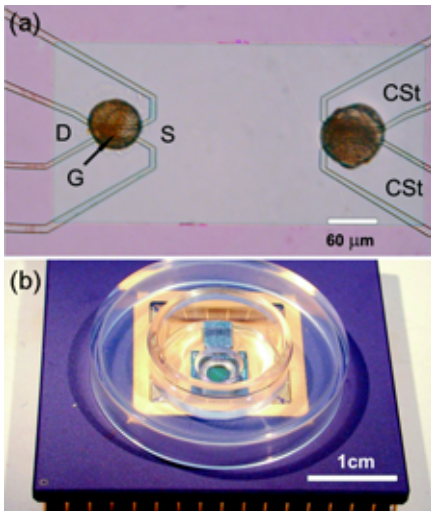
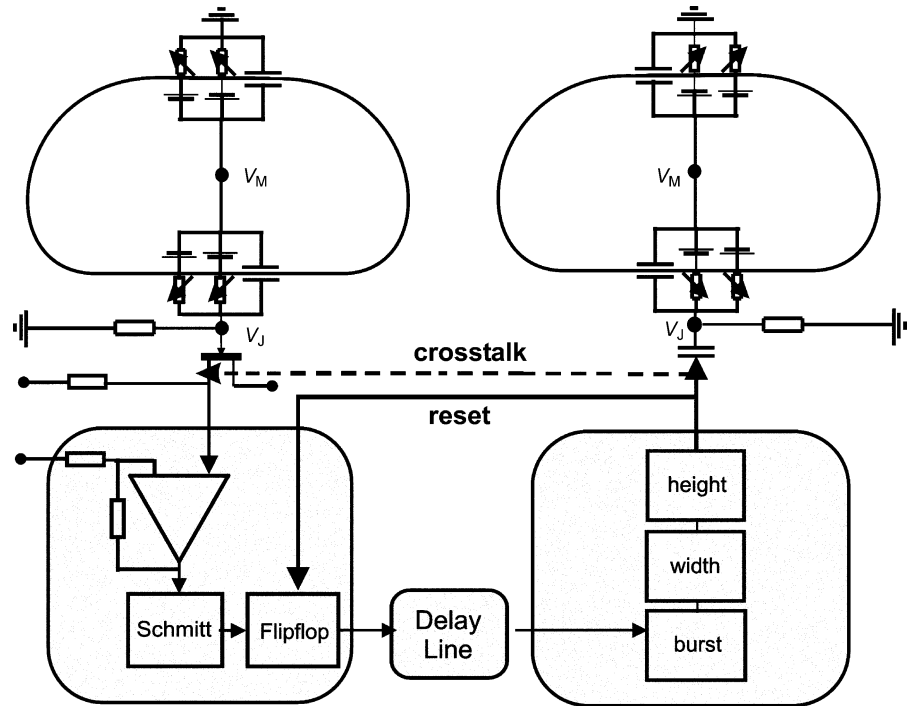


**Figure 20:** Neurochip.

(a) Micrograph of a silicon chip with an all-silica surface. Two snail neurons are attached to two two-way interface contacts. The source (S), drain (D) and gate (G) of a transistor, and the wings of a capacitive stimulator (CSt) are marked [32]. The surface of the chip is made of silicon dioxide. The bright rectangle is the area of thin oxide.

(b) Perspex chamber with chip. The quadratic interface unit forms the bottom of the circular perspex chamber in contact to the culture medium. The interneuron unit is bonded to it side by side, shielded from the electrolyte.

delay line is started. (iv) A train of voltage pulses is generated and applied to a capacitive stimulator. (v) The crosstalk from stimulator to transistor in the chip is eliminated by a refractory circuit: the delay line is not started directly by the output of the Schmitt-trigger, but by the onset of a flip-flop as triggered by an action potential. The flip-flop is reset after stimulation.

In a first implementation, the chip consists of two parts, an interface unit with transistors and stimulation spots and an interneuron unit implemented as a conventional integrated circuit for discrimination, delay line and pulse shaping [31], [32]. Figure 20a shows two snail neurons attached to two-way contacts of the interface unit. The two silicon chips of the interfacing and the interneuron unit are bonded side by side with the interface unit exposed to the culture medium in a chamber as illustrated in Figure 20b.

The connection from a spontaneously firing neuron A along the chip to a separated neuron B is shown in Figure 21. Both neurons are impaled by micropipette electrodes to observe their intracellular voltage  $V_M$ . On the left we see four action potentials of neuron A and the response of the transistor after amplification. The negative transient of the source-drain current is caused by an outward current through the cell membrane. On the right we see four delayed bursts of voltage pulses (17 pulses, height 2 V, width 0.3 ms, interval 0.3 ms) that are applied to the stimulator beneath neuron B. The firing of neuron B is in strict correlation to the firing of neuron A.

The first step of processing on the chip is the assignment of a digital signal to each action potential of neuron A (Figure 21). However, in addition the transistor records strong short perturbations in coincidence with the stimulation pulses at neuron B. They are caused by capacitive crosstalk on the chip. A digital signal is assigned to these artifacts, too, as shown in Figure 21. A second processing step on the chip prevents these artifacts from feeding back into the pulse generator: the response to each action potential activates a flip-flop (Figure 21). The onset of the flip-flop starts the delay line that triggers the voltage generator. The flip-flop is reset after completed stimulation. Thus the stimulation artifact meets an activated flip-flop and cannot interfere.

The pathway neuron – silicon – neuron demonstrates that single action potentials from individual nerve cells can be reliably fed into a digital electronic processor, and that after computations a single action potential in an individual nerve cell can be reliably elicited, all on a microscopic level. The study relies on the established physiology of

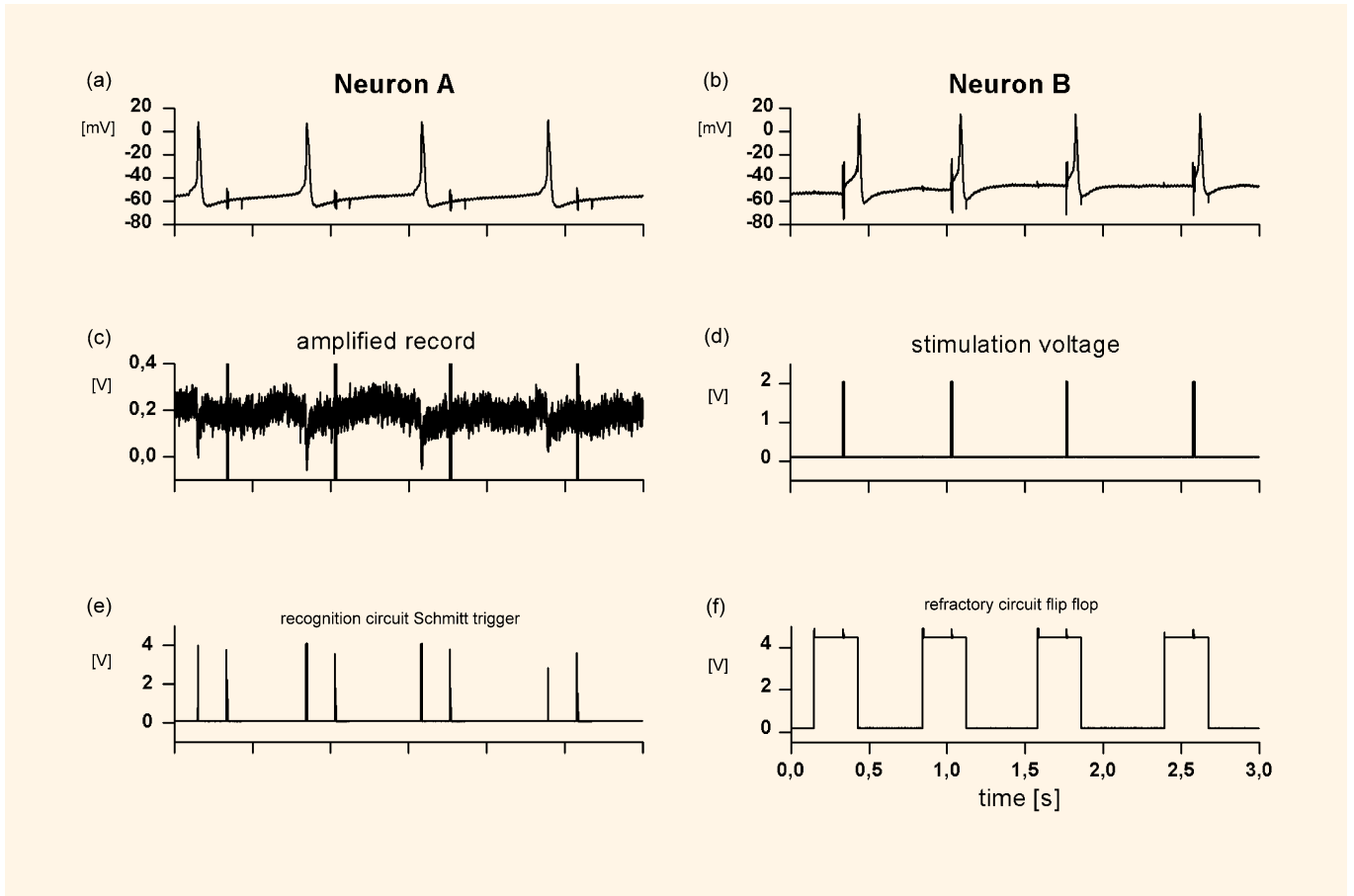


**Figure 21:** Pathway neuron-silicon chip-neuron [32].

- (a) Intracellular voltage of neuron A.
- (b) Intracellular voltage of neuron B which fires with a constant delay after neuron A.
- (c) Response of the transistor beneath neuron A after current-voltage conversion and amplification. Weak downward signals of the action potentials and strong perturbations due to cross talk of the stimulation voltages at neuron B.
- (d) Bursts of voltage pulses at the stimulator beneath neuron B. Each burst of 10 ms duration consists of 17 voltage pulses (width and separation 0.3 ms).
- (e) Output of the Schmitt trigger. Signals are assigned to the action potentials and to the cross-talk perturbations.
- (f) State of the refractory flip-flop. The flip-flop is set by an action potential. This transition triggers the delay line that elicits the stimulation voltages. It is reset after the end of the stimulation burst.

neurons, on the known physics of interfacing and on standard electronics. It is a fundamental exercise in neuroelectronic engineering. The crosstalk may be avoided (i) by an enhanced capacitance of the stimulators and a lower amplitude of the stimulation pulses, (ii) by transistors with lower noise to provide better defined waveforms of the records such that they can be distinguished from artifacts and (iii) by blocking devices on the chip to reduce the interferences.

**Electrical synapses.** Neuronal networks rely on synaptic connections. In a first stage we use nerve cells from the snail *Lymnaea stagnalis* which form strong electrical synapses [33]. In these contacts electrical current flows from the presynaptic to the postsynaptic cell through the gap junctions that bridge both cell membranes. An electrical synapse transmits current of hyperpolarisation. The transmission of a stationary presynaptic hyperpolarization  $\Delta V_M^{(pre)}$  to a postsynaptic hyperpolarization  $\Delta V_M^{(post)}$  defines the coupling coefficient  $k_{pre,post}$  according to (34).

$$k_{pre,post} = \frac{\Delta V_M^{(pre)}}{\Delta V_M^{(post)}} \quad (34)$$

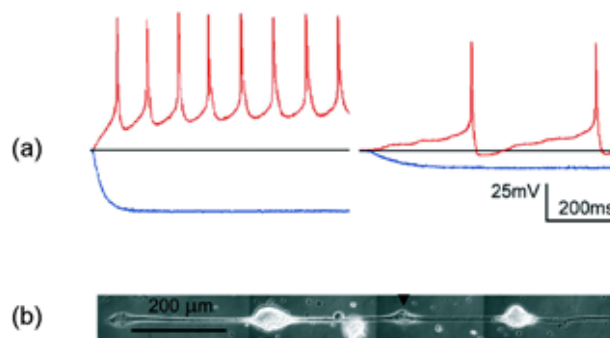
A pair of snail neurons with a coupling coefficient  $k_{pre,post} = 0.29$  is shown in Figure 22 for two neurons grown on a linear pattern [33]. The left neuron is stimulated by an impaled micropipette, the pre- and postsynaptic membrane potentials are measured with impaled pipettes. Apparently, the synapse transmits a hyperpolarization. When the left neuron is stimulated by depolarizing current, a train of action potentials is elicited. Each action potentials injects current into the postsynaptic cell such that after four spikes the threshold is reached of an action potential in the postsynaptic neuron.

**Immobilization of neurons.** An electronic supervision of neuronal nets requires a precise placement of the cells on two-way contacts and a “wiring” by neurites that form synaptic connections. However, when the snail neurons are attached to defined sites of a

**Figure 22:** Electrical synapse between two neurons [33].

(a) Electrical signal transfer from the left to the right neuron. In blue, transmission of hyperpolarization, in red, transmission of neuronal activity.

(b) Micrograph of two snail neurons grown on a linear lane forming an electrical synapse (marked with a triangle).



chip, the sprouting neurites exert strong forces on the cell bodies. As a result the cells are displaced from their contact sites [34]. An example is shown in Figure 23. Several neurons are attached to two-way contacts in a circular arrangement. Within two days a network of neurites is formed in the central area of the chip where the neurons are connected by electrical synapses. But the cell bodies are removed from their two-way contacts. The mechanical instability of the arrangement dramatically lowers the yield of a simultaneous interfacing of two neurons.

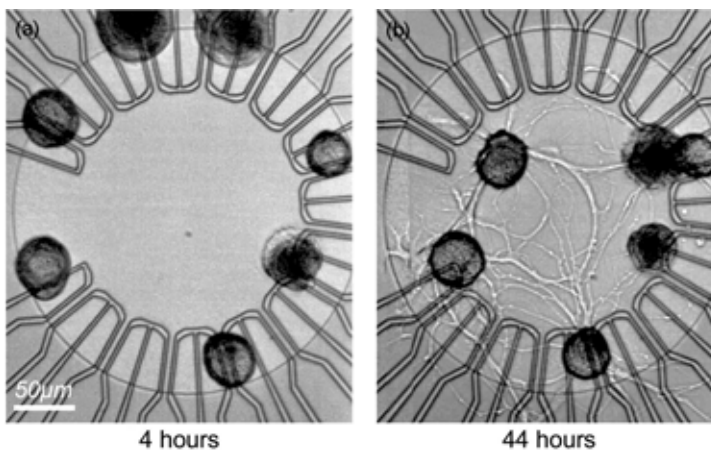
The problem of displacement is overcome by a mechanical fixation of the cell bodies. Picket fences are fabricated around each two-way contact by photolithography of a polyimide [35]. Neuronal cell bodies are inserted into the cages as illustrated in Figure 24a. They are immobilized even after extensive outgrowth. A chip with a network on a circular array of two-way contacts is shown in Figure 24b.

Mechanical immobilization allows an interfacing of more than one neuron in a net with sufficient probability. Two aspects of the technology are crucial: (i) The fabrication of the cages is a low-temperature process and does not interfere with the semiconductor devices. (ii) The neurites grow on the same surface where the cell bodies are attached. No forces arise that lift the cell bodies from the two-way contacts.

**Signaling chip-neuron-neuron-chip.** An experiment with a signaling pathway silicon-neuron-neuron-silicon (Figure 14) is shown in Figure 25 using a network of immobilized snail neurons [35]. Two neurons are selected which are connected by an electrical synapse and which are placed on two-way junctions. A burst of seven pulses is applied to excite neuron 1 as checked with an impaled micropipette. In neuron 2 we observe a subthreshold postsynaptic depolarization. A second burst of voltage pulses elicits another action potential in neuron 1 and leads to a further depolarization of neuron 2. After the third burst, which fails to stimulate neuron 1, the fourth burst gives rise to an

**Figure 23:** Displacement of neuronal cell bodies by neuronal outgrowth [34]. Snail neurons are placed on a chip with a circular array of two-way contacts. The chip is coated with polylysine and the culture medium is conditioned with snail brains.

(a) 4 hours after mounting.  
(b) 44 hours after mounting.



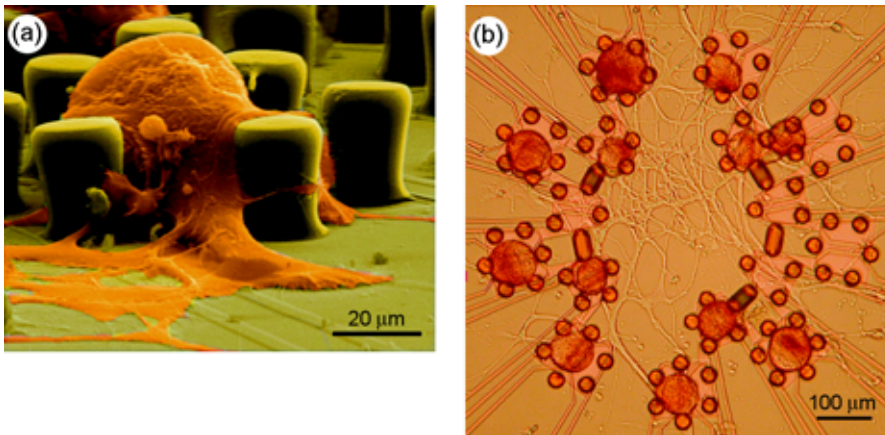


**Figure 24:** Mechanically stabilized network of neurons on silicon chip [35]. (a) Electron micrograph of a snail neuron immobilized by a picket fence on a two-way contact after three days in culture. Scale bar 20  $\mu\text{m}$ . (b) Micrograph of neuronal net with cell bodies (dark blobs) on a double circle of two-way contacts with neurites grown in the central area (bright threads) after two days in culture. Scale bar 100  $\mu\text{m}$ . Pairs of pickets in the inner circle are fused to bar-like structures.

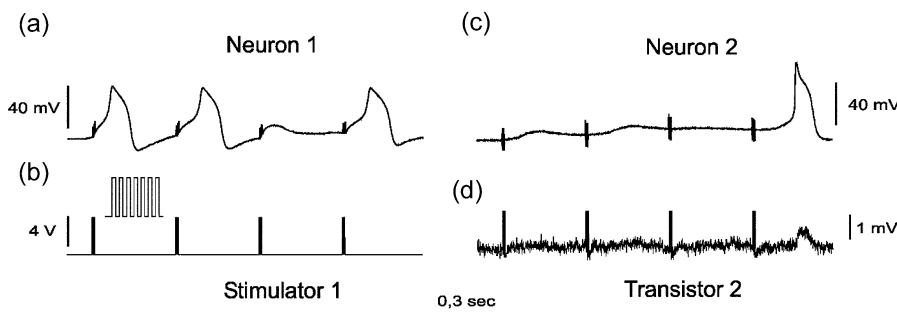


**Figure 25:** Electronic interfacing of two synaptically connected snail neurons [35]. (a) Intracellular voltage of neuron 1. (b) Bursts of voltage pulses applied to the stimulator (seven pulses, amplitude 5 V, duration 0.5 ms). (c) Intracellular voltage of neuron 2. (d) Transistor record of neuron 2.

action potential in neuron 1 which finally leads to a postsynaptic excitation in neuron 2. That postsynaptic action potential is recorded by the transistor underneath neuron 2, completing an electronically interfaced monosynaptic loop.

Correlated with the burst of stimulation pulses, we observe perturbations of the transistor records and of both microelectrode signals. These perturbations do not reflect actual changes of the voltage on the gate or of the intracellular voltage, respectively. Control experiments without neurons reveal a direct pathway of capacitive coupling through the chip from stimulators to transistors. Control experiments with an open stimulator and a neuron far away reveal a capacitive coupling to the micropipette through the bath. A subsequent depolarization of the cell is not observed in that case. On the other hand the shape, the delay and the temporal summation of the postsynaptic signals correspond to the experiments with intracellular presynaptic stimulation (Figure 22). We conclude that the depolarization of the postsynaptic neuron in Figure 25 is induced by synaptic transmission and not by direct chip stimulation.

### 3.4 Towards defined Neuronal Nets

The function of neuronal networks is generally based on two features: (i) A mapping of a set of neurons onto another set or a mapping of a set of neurons onto itself as in the symmetrical Hopfield net illustrated in Figure 26. (ii) Hebbian learning rules with an enhancement of synaptic strength as a consequence of correlated presynaptic and postsynaptic activity. Systematic experiments on network dynamics require (i) a noninvasive supervision of all neurons with respect to stimulation and recording to induce learning and to observe the performance of the net on a long time scale, and (ii) a fabrication of neuronal maps with a defined topology of the synaptic connections. To achieve the second goal we have to control neuronal outgrowth, the direction and bifurcation of neurites and the formation synapses.

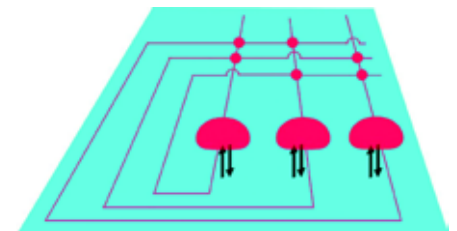


**Figure 26:** Defined neuronal network (red) with symmetrical connections of axons, synapses and dendrites supervised from a semiconductor chip (blue) by two-way interfacing (black).

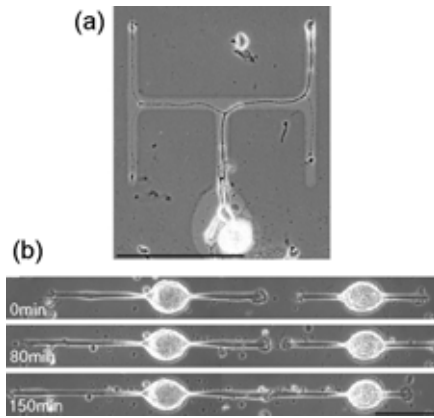


**Figure 27:** Guided outgrowth by chemical patterns [33], [37].  
 (a) Defined bifurcations of a leech neuron. The pattern with orthogonal branchings is made by UV photolithography of extracellular matrix protein. Scale bar 100  $\mu\text{m}$ .  
 (b) Controlled formation of a synapse between two snail neurons. The lanes are made by UV photolithography of brain derived protein adsorbed to the substrate. Scale bar 100  $\mu\text{m}$ .

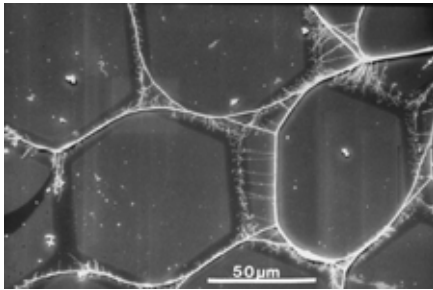


**Figure 28:** Incomplete control by chemical guidance [36]. Electronmicrograph of the neurites of leech neurons. Scale bar 50  $\mu\text{m}$ . A hexagonal pattern of extracellular matrix protein is made by UV photolithography. Grown neurites dissociate from the guiding lanes. Neurites grow without control on all given lanes of the pattern.

**Chemical guidance.** The motion of neuronal growth cones is guided by chemical patterns. Defined arborizations of leech neurons are achieved by chemical guidance with lanes of extracellular matrix protein [37], [38]. They are fabricated by UV photolithography of a homogeneous film of extracellular matrix protein using metal masks. When a cell body is placed on the root of a tree-like pattern with orthogonal branchings, the growth cone perfectly follows the lanes and is perfectly split at the branch points into daughter cones as illustrated in Figure 27a.

Using linear chemical patterns, we are able to guide the outgrowth of two neurons such that their growth cones are forced to collide and to form a synapse. That experiment is performed with snail neurons [33]. The chip is coated with polylysine and incubated with dissected snail brains. Secreted proteins are adsorbed on the chip and patterned by UV photolithography. Three stages are illustrated in Figure 27b. After the encounter of the growth cones, synapse formation is checked as discussed above.

Though the process of chemical guidance is rather perfect, there are two problems: (i) The stability of neuritic trees is limited. Neurites have a tendency to shorten. When they are guided around a corner, they dissociate from the guiding lane and cross the non-guiding environment. (ii) A patterned substrate provides a restricted area of growth, but it does not guide a neurite in a certain direction on a branched pattern; with several neurons it does not guide a certain neuron into a certain direction. These two problems of chemical guidance are illustrated in Figure 28 with leech neurons on a hexagonal pattern [36].

Apparently, neuronal growth cones are perfectly guided by the lanes of extracellular matrix protein. But, grown neurites dissociate from the bent lanes such that the defined shape of the neuritic tree is lost. Different neurites grow on the same lane, such that the neuritic tree is not defined by the pattern.

**Topographical guidance.** The instability of grown neuritic trees is overcome by topographical guidance. There the grown neurites are immobilized by microscopic grooves which are used as cues for the guidance of the growth cones. Microscopic grooves are fabricated from a polyester photoresist on the chip [38]. An example of a topographical structure obtained by photolithography with five pits and connecting grooves is depicted in Figure 29a. The resin is compatible with cell culture and the low temperature process does not damage microelectronic devices of the chip. The insert of Figure 29a shows the perfectly vertical walls of the pits and grooves.

The chip is coated with polylysine. Secreted proteins from excised snail brains in the culture medium are adsorbed and render the surface of silicon dioxide on the bottom of grooves and pits as well as the surface of the polyester equally suitable for outgrowth. Cell bodies of snail neurons are placed into the pits of the polymer structure. Neurites grow along the grooves and are split at bifurcations of the groove to form neuritic trees as shown in Figure 29b. Because a micrograph does not allow an assignment of the neurites to the different neurons, we sequentially stain individual neurons by injection with the dye Lucifer Yellow which cannot pass the electrical synapses of snail neurons. The synaptic connections are checked by impaling with micropipettes as discussed above.

**Electrical guidance.** Topographical guidance does not solve the problem, that a neuritic tree is not uniquely defined by the guiding pattern. We must combine it with control signals that are only effective at certain positions and certain times to promote or inhibit the growth at a crossing or a branch points and that induce or prevent synapse formation at certain places. Electrical manipulation of growth cones may be a tool to accomplish that task [39].

**Conclusion.** In a next step, we can envisage joining small networks with defined geometry - made by chemical, mechanical or electrical guidance - to silicon chips with two-way contacts. It remains unclear, however, whether large neuronal nets with hundreds and thousands of neurons can be joined in a defined way by the various methods of guidance. An alternative strategy may be kept in mind, the outgrowth of a disordered neuronal net on a chip with thousands of closely packed interface structures. There most neurons would be on a contact at any time and the rearranging network would be continuously supervised in its structure and dynamics.

## 4 Brain-Silicon Chips

Instead of culturing defined neuronal nets by controlled outgrowth, we may use neuronal nets given by brains. Considering the planar nature of semiconductor chips, planar networks are preferred in order to attain an adequate supervision by the chip. Organotypic

brain slices are particularly promising as they are only a few cell layers thick and conserve major neuronal connections. A cultured slice from rat hippocampus on a chip with a linear transistor array is shown in Figure 30. When we succeed in coupling a brain-grown net to numerous, closely packed transistors and stimulation spots, we are able to study the distributed dynamics of the neuronal network.

An interfacing of a transistor or stimulation spot with an individual neuron in neuronal tissue can hardly be achieved. Thus with brain slices, we have to consider the stimulation and recording of local populations of neurons. The concept of a core-coat conductor of individual cells is not adequate. To guide the development of appropriate chips and to evaluate experimental data, we discuss an approach that relates (i) neuronal currents in a slice to the extracellular potential that is recorded by transistors and (iii) the capacitive stimulation currents from a chip to the extracellular potential that elicits neuronal excitation of the tissue [40]. On that basis, we consider first experiments with transistor recording in brain slices [41] and the implications of capacitive stimulation.

## 4.1 Tissue-Sheet Conductor

In an organotypic brain slice, the neurons are embedded in a tissue of about  $100\ \mu\text{m}$  thickness between the insulating silicon dioxide of a chip and an electrolytic bath on ground potential as illustrated in Figure 31a. Excited neurons are local sources or sinks of current that flows to adjacent regions of the tissue layer and to the bath. As a consequence, an extracellular potential appears in the tissue that may be recorded by transistors in the substrate. On the other hand, capacitive contacts in the substrate may locally inject current into the tissue layer, that flows to adjacent regions of the slice and to the bath. The resulting extracellular potential may elicit neuronal excitation. In contrast to the studies with individual neurons, we have to deal here with the stimulation and recording of neuronal populations.

**Volume conductor.** In a tissue of densely packed neurons, we do not consider the true extracellular voltage on a submicrometer level between the cells, but an average field potential  $V_{\text{field}}$  that arises from currents per unit volume  $j_{\text{source}}$  of cellular sources or  $j_{\text{stim}}$  due to stimulation electrodes. The continuity relation of current in three dimension leads to (35) with the three-dimensional spatial derivative operator  $\nabla$  assuming an isotropic average specific resistance  $\rho$  of the tissue.

$$-\nabla \left( \frac{1}{\rho} \nabla V_{\text{field}} \right) = j_{\text{stim}} + j_{\text{source}} \quad (35)$$

We have to consider two boundary conditions [40]: (i) The slice is on ground potential at its surface. With the  $z$ -direction normal to the layer plane and a height  $h$  of the slice, the constraint is  $V_{\text{field}}(h) = 0$  at  $z = h$ , when we neglect voltage drops in the bath. (ii) At the substrate, the capacitive current per unit area  $j_{\text{stim}}^{(2)}$  determines the gradient of the potential with  $-(dV_{\text{field}}/dz)_0 = \rho j_{\text{stim}}^{(2)}$  at  $z = 0$ . In principle, the field potential can be computed from (35) with the boundary conditions for an arbitrary pattern of stimulation electrodes and an arbitrary distribution of neuronal excitation. However, to get a simple picture of the electrical properties of a slice, we consider a two-dimensional model based on the volume conductor theory.

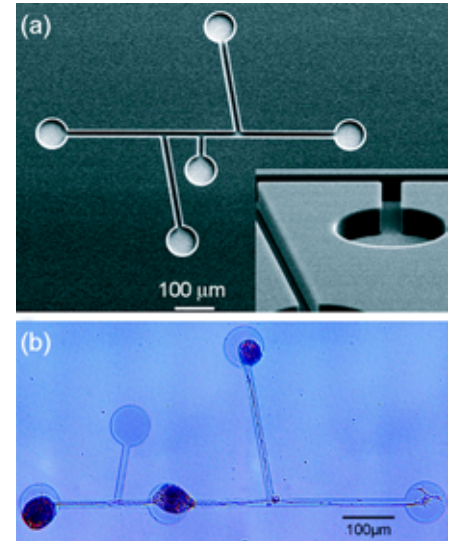
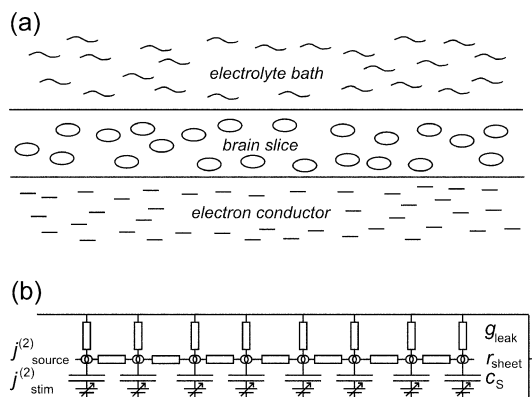


**Figure 29:** Topographical guidance [38]. (a) Polyester structure on silicon chip with pits and grooves. Electronmicrograph, scale bar  $100\ \mu\text{m}$ . (b) Micrograph of a network of three snail neurons formed by topographical guidance. The neurons are connected by electrical synapses.

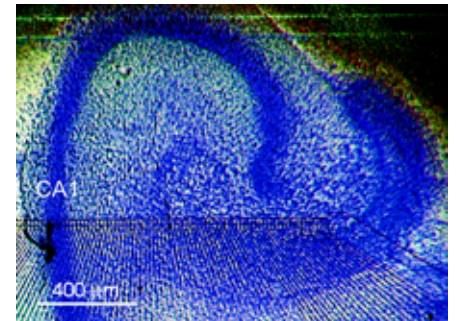


**Figure 30:** Organotypic slice from rat hippocampus on silicon chip [41]. Nissl staining of a slice cultured for 14 days. Scale bar  $400\ \mu\text{m}$ . The dots are neuronal cell bodies. A linear array of field-effect transistors is aligned perpendicular to the CA1 region through the stratum pyramidale and the stratum radiatum until the gyrus dentatus (see text).

**Figure 31:** Brain slice on silicon substrate [40]. (a) Geometry of tissue layer between electron conductor and electrolyte bath. (b) Sheet conductor model. The neurons in the slice give rise to a current-source density per unit area  $j_{\text{source}}^{(2)}$ . The current flows along the slice (sheet resistance  $r_{\text{sheet}}$ ) and to the bath ( $g_{\text{leak}}$ , leak conductance). The slice is stimulated by a current density  $j_{\text{stim}}^{(2)}$  from the chip by capacitive contacts (specific capacitance  $c_s$ ).

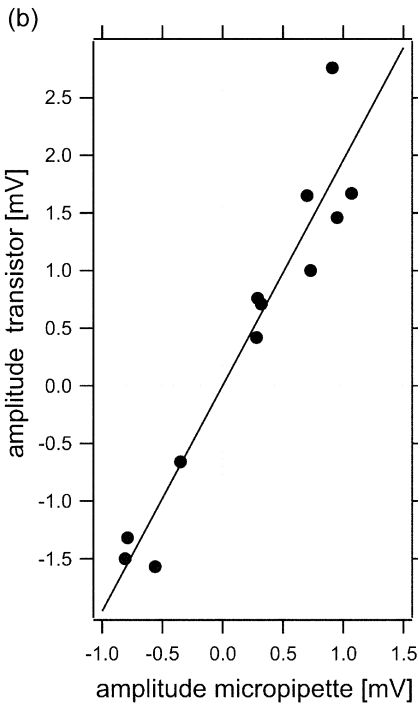
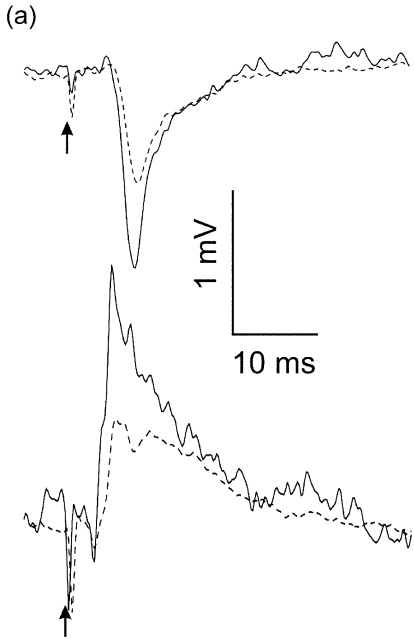


**Figure 32:** Transistor recording in organotypic slice of rat hippocampus [41].

(a) Evoked field potentials in the stratum radiatum (top) and stratum pyramidale (bottom) of the CA1 region. The arrows mark the stimulation artifact. The dashed lines are the simultaneous records by micropipette electrodes.

(b) Amplitude of transistor records versus amplitude of microelectrodes. The regression line has a slope of 1.96.

**Sheet-conductor model.** A brain slice between chip and bath is a planar conductor with a capacitive bottom and a leaky cover. Neglecting the  $z$ -dimension normal to the plane, we describe the thin tissue by a sheet resistance  $r_{\text{sheet}}(x,y)$ , the shunting effect of the bath by an ohmic conductance per unit area  $g_{\text{leak}}(x,y)$ , and the substrate by a capacitance per unit area  $c_S(x,y)$  as illustrated by the circuit of Figure 31b. The neuronal current sources per unit area  $j_{\text{source}}^{(2)}(x,y)$  and the stimulation current due to a changing voltage  $V_S$  at the capacitive contacts are balanced by the current along the sheet and by ohmic and capacitive shunting to bath and substrate according to (35) with the potential  $V_{\text{field}}(x,y)$  and the 2-D spatial derivative operator  $\nabla$ .

$$-\nabla \left( \frac{1}{r_{\text{sheet}}} \nabla V_{\text{field}} \right) + g_{\text{leak}} V_{\text{field}} = j_{\text{source}}^{(2)} + c_S \left( \frac{\partial V_S}{\partial t} - \frac{\partial V_{\text{field}}}{\partial t} \right) \quad (36)$$

The sheet conductor model formulated by (36) describes (i) the extracellular field potential that arises from neuronal activity with  $\partial V_S / \partial t = 0$ , as it may be recorded with transistors, and (ii) the extracellular field potential that is caused by capacitive stimulation with  $j_{\text{source}}^{(2)}(x,y) = 0$ , as it may elicit neuronal excitation.

Note the similarity and the difference between Figure 31b with (36) and Figure 4a with (1): In both cases the circuits and the differential equations describe the continuity relation of electrical current in a two-dimensional system. However, Figure 4a and (1) refer to the junction of an individual cell and a chip, whereas Figure 31b and (36) describe a tissue sheet with numerous neurons on a chip.

## 4.2 Transistor Recording of Brain Slice

We culture a slice from rat hippocampus on a silicon chip with an all-oxide surface and a linear array of transistors as shown in Figure 30. The slice has a thickness  $h = 70 \mu\text{m}$ . It is stimulated with a tungsten electrode in the gyrus dentatus. A profile of evoked field potentials is recorded across the CA1 region [41].

**Field potential.** Two transistor records from the stratum radiatum (layer of dendrites) and from the stratum pyramidale (layer of cell bodies) are shown in Figure 32a. Excitatory postsynaptic potentials of neuronal populations are observed. There is a negative amplitude in the region of the dendrites where current flows into the cells and a positive amplitude in the region of the cell bodies with a compensating outward current. For comparison the records of micropipette electrodes are plotted in Figure 32a. The transistor records have an identical shape, but a higher amplitude than the micropipette records. The amplitudes are proportional to each other as shown in Figure 32a. The identical shape and the similar and proportional amplitude validate the approach of transistor recording. Larger amplitudes are expected for a measurement near the insulating substrate where the shunting effect of the bath is smaller as compared to a measurement near the surface where the microelectrodes are positioned.

**Potential profile across CA1.** The amplitudes of the evoked field potentials across the CA1 region are plotted versus the position of the transistors in Figure 33 [41]. The region of negative potentials matches the stratum radiatum, the region of positive potentials the stratum pyramidale.

We evaluate the experimental field potential with the sheet-conductor model. Along the CA1 layer of the hippocampus the electrical activity is usually assumed to be constant. In that case (36) can be reduced to a one-dimensional relation across the CA1 region along the soma-dendrite direction  $x$ . Without stimulation we obtain (37) with the length constant  $\lambda_{\text{sheet}} = 1/\sqrt{g_{\text{leak}} r_{\text{sheet}}}$  when we neglect the capacitive current with  $c_S dV_{\text{field}}/dt \ll g_{\text{leak}} V_{\text{field}}$ .

$$-\lambda_{\text{sheet}}^2 \frac{d^2 V_{\text{field}}}{dx^2} + V_{\text{field}} = \frac{j_{\text{source}}^{(2)}}{g_{\text{leak}}} \quad (37)$$

We express the sheet resistance as  $r_{\text{sheet}} = \rho/h$  by the specific resistance of the slice and its thickness and the leaks as  $g_{\text{leak}} = 2/\rho h$  by the conductance from the center of the slice to the bath. The length constant is  $\lambda_{\text{sheet}} = h/\sqrt{2}$ .

The simplest current profile that is physiologically meaningful is a constant density of synaptic inward current in the stratum radiatum that is balanced by a constant outward current density in the stratum pyramidale. For a constant current-source density  $j_{\text{source}}^{(2)}$  in a range  $-x_0 < x < x_0$ , the field potential is given by (38).

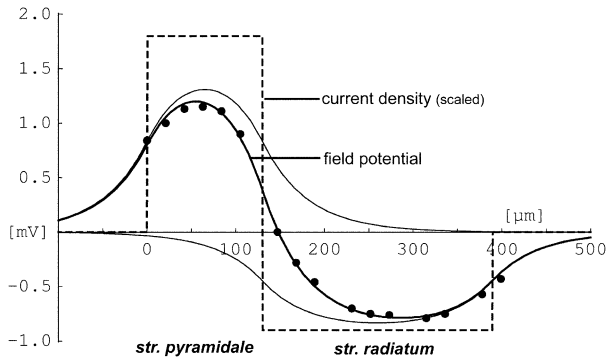


**Figure 33:** Profile of evoked field potentials across the CA1 region [41]. The amplitude of voltage transients is plotted versus the position of the transistors (black dots). The data are fitted with the field potential  $V_{\text{field}}$  computed by the sheet conductor model with a constant negative current density in the stratum radiatum and a balancing constant positive current density in the stratum pyramidale. The contributions from the two strata are drawn as thin lines. The scaled profile of current density  $j_{\text{source}}^{(2)}/g_{\text{sheet}}$  is indicated (dashed line).

$$V_{\text{field}}(x) = \frac{j_{\text{source}}^{(2)}}{g_{\text{leak}}} \begin{cases} 1 - \exp\left(-\frac{x_0}{\lambda_{\text{sheet}}}\right) \cosh\left(\frac{|x|}{\lambda_{\text{sheet}}}\right) & |x| < x_0 \\ \sinh\left(\frac{x_0}{\lambda_{\text{sheet}}}\right) \exp\left(-\frac{|x|}{\lambda_{\text{sheet}}}\right) & |x| > x_0 \end{cases} \quad (38)$$

The width of the stratum radiatum is about 260  $\mu\text{m}$ , of the stratum pyramidale about 130  $\mu\text{m}$ . Using (38) we compute the potential profile of the two regions and superpose them. We obtain a perfect fit of the experimental data with  $\lambda_{\text{sheet}} = 50 \mu\text{m}$  choosing scaled current densities  $j_{\text{source}}^{(2)}/g_{\text{leak}} = -0.9 \text{ mV}$  in the stratum radiatum and  $j_{\text{source}}^{(2)}/g_{\text{leak}} = 0.9 \text{ mV}$  ( $260 \mu\text{m}/130 \mu\text{m}$ ) = 1.8 mV in the stratum pyramidale as shown in Figure 33. In the center of the stratum radiatum the curvature of the field potential  $V_{\text{field}}(x)$  is small. Considering (37), there the potential reflects the synaptic current density with  $V_{\text{field}} \propto j_{\text{source}}^{(2)}$ . This result is in contrast to the volume conductor theory for bulk brain where the curvature is proportional to the local current source density according to (36).

### 4.3 Capacitive Stimulation of Brain Slices

In a next step we will implement the stimulation of brain slices from silicon chips. The sheet conductor model is a useful guide to develop optimal capacitive contacts.

**Circular contact.** We consider the capacitive stimulation through a circular stimulation spot. From (36) we obtain (39) for a homogeneous slice in cylinder coordinates with the radius coordinate  $a$  when we disregard neuronal activity and assume  $dV_{\text{field}}/dt \ll dV_S/dt$  [40].

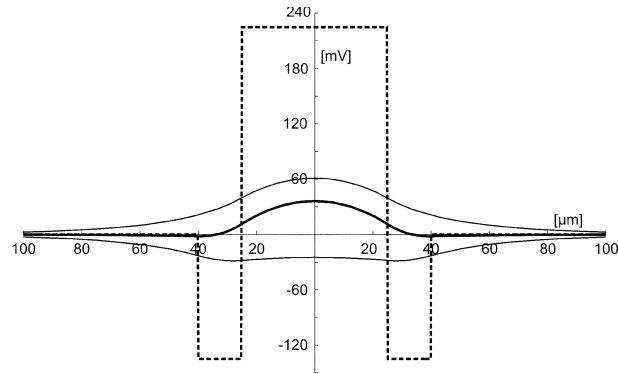
$$-\lambda_{\text{sheet}}^2 \left( \frac{\partial^2 V_{\text{field}}}{\partial a^2} + \frac{1}{a} \frac{\partial V_{\text{field}}}{\partial a} \right) + V_{\text{field}} = \frac{c_S}{g_{\text{leak}}} \frac{\partial V_S}{\partial t} \quad (39)$$

For a stationary stimulation  $dV_S/dt = \text{const.}$  with a capacitive contact  $c_S \neq 0$  for  $a < a_0$  we obtain (40) with the modified Besselfunctions  $I_0, I_1, K_0,$  and  $K_1$ .

$$V_{\text{field}}(a) = \frac{c_S}{g_{\text{leak}}} \frac{dV_S}{dt} \begin{cases} 1 - \frac{a_0}{\lambda_{\text{sheet}}} K_1\left(\frac{a_0}{\lambda_{\text{sheet}}}\right) I_0\left(\frac{a}{\lambda_{\text{sheet}}}\right) & a < a_0 \\ \frac{a_0}{\lambda_{\text{sheet}}} I_1\left(\frac{a_0}{\lambda_{\text{sheet}}}\right) K_0\left(\frac{a}{\lambda_{\text{sheet}}}\right) & a > a_0 \end{cases} \quad (40)$$

The field potential for a radius  $a_0 = 25 \mu\text{m}$  is drawn in Figure 34 with  $\lambda_{\text{sheet}} = 35 \mu\text{m}$ ,  $r_{\text{sheet}} = 60 \text{ k}\Omega$  and  $g_{\text{leak}} = 13.3 \text{ nS}/\mu\text{m}^2$ . These parameters correspond to a thickness  $h = 50 \mu\text{m}$  and a specific resistance  $\rho = 300 \Omega\text{cm}$ . We apply a voltage ramp for 100  $\mu\text{s}$  with an amplitude of 1 V to a contact with a capacitance  $c_S = 30 \mu\text{F}/\text{cm}^2$ .

**Figure 34:** Theory for capacitive stimulation of brain slice [40]. Field potential versus electrode radius computed for a length constant  $\lambda_{\text{sheet}} = 35 \mu\text{m}$ . The central area has a radius of  $25 \mu\text{m}$ , a ring-shaped surround a width of  $15 \mu\text{m}$ . The scaled stimulation current per unit area  $(c_S/g_{\text{leak}})dV_S/dt$  is indicated as a dashed line. The potential profile  $V_{\text{field}}(a)$  due to center-surround stimulation is plotted (heavy line), as well the profiles due to positive stimulation in the center (upper thin line), and negative stimulation in the surround (lower thin line).



The field potential is not localized but spreads far beyond the contact area. The maximum amplitude in the center of the contact is around 60 mV, far lower than the amplitude  $(c_S/g_{\text{leak}})dV_S/dt = 225 \text{ mV}$  that would be attained for an infinitely large electrode. The localization of the field potential can be improved by a negative stimulation in a circular surround as illustrated in Figure 34. The improved localization, however, leads to a further reduction of the amplitude. On the basis of these computations, adequate capacitive contacts on silicon chips have to be developed.

## 5 Summary and Outlook

The present paper shows that the basic questions on the electrical interfacing of individual nerve cells and semiconductor chips are fairly well answered, the nature of the core-coat conductor, the properties of the cleft, the role of accumulated ion channels, the mechanism of transistor recording and capacitive stimulation. With respect to the latter issue, however, studies on the capacitive gating of ion channels and on electroporation on planar stimulation contacts are required. In the near future, we are faced with important steps of optimization: (i) On the side of the semiconductor, the capacitance of the stimulation contacts must be enhanced and the noise of the transistors has to be lowered. (ii) On the side of the neurons, the structural and electrical properties of the cell membrane (glyocalix, ion channels) in the neuron-semiconductor junction must be studied and optimized by recombinant methods.

With respect to systems of neuronal networks and digital microelectronics, we are in a rather elementary stage. Two directions may be envisaged in the future: (i) Small defined networks of neurons from invertebrates and mammals must be created with learning chemical synapses and with a defined topology of synaptic connections. (ii) Large neuronal nets may be grown on closely packed arrays of two-way interface contacts, such that the rearranging structure and dynamics of the net is under continuous control of the chip. An adaptation of the industrial standard of *CMOS* technology will be crucial.

The interfacing of brain slices is in its infancy. In the near future, the two-way interfacing of groups of neurons in a tissue has to be studied in detail. Then two directions must be followed: (i) Arrays of two-way contacts will lead to a complete spatiotemporal mapping of brain dynamics. (ii) Learning networks on a chip will be implemented and will allow systematic studies of memory formation.

The availability of involved integrated neuroelectronic systems will help to unravel the nature of information processing in neuronal networks and will give rise to new and fascinating physical-biological-computational questions. Of course, visionary dreams of bioelectronic neurocomputers and microelectronics neuroprostheses are unavoidable and exciting, but they should not obscure the numerous practical problems.

## Acknowledgements

The work reported in this chapter was possible only with the cooperation of numerous students who contributed with their skill and enthusiasm. Most valuable was also the help of Bernt Müller (Institute for Microelectronics, Technical University Berlin) who fabricated several chips and gave his advice for our own chip technology. The neurochip project was generously supported by the University Ulm, the Fonds der Chemischen Industrie, the Deutsche Forschungsgemeinschaft, the Max-Planck-Gesellschaft and the Bundesministerium für Bildung und Forschung. The editor acknowledges Christiane Hofer (RWTH Aachen) for checking the comprehensive set of symbols and formulas in this chapter. Furthermore, he would like to thank Matthias Schindler (RWTH Aachen) for checking the clarity and consistency of this chapter.

## References

- [1] P. Fromherz, 20<sup>th</sup> Winterseminar “Molecules, Memory and Information“, Klosters 1985. (Available at [http://www.biochem.mpg.de/mnphys/.](http://www.biochem.mpg.de/mnphys/))
- [2] P. Fromherz, A. Offenhäusser, T. Vetter, J. Weis, *Science* **252**, 1290 (1991).
- [3] P. Fromherz, A. Stett, *Phys. Rev. Lett.* **75**, 1670 (1995).
- [4] A. Lambacher, P. Fromherz, *Appl. Phys. A* **63**, 207 (1996).
- [5] A. Lambacher, P. Fromherz, *J. Opt. Soc. Am.* **B19**, 1435 (2002).
- [6] D. Braun, P. Fromherz, *Appl. Phys. A* **65**, 341 (1997).
- [7] D. Braun, P. Fromherz, *Phys. Rev. Lett.* **81**, 5241 (1998).
- [8] Y. Iwanaga, D. Braun, P. Fromherz, *Eur. Biophys. J.* **30**, 17 (2001).
- [9] P. Fromherz, C.O. Müller, R. Weis, *Phys. Rev. Lett.* **71**, 4079 (1993).
- [10] R. Weis, P. Fromherz, *Phys. Rev.E* **55**, 877 (1997).
- [11] M. Brittinger, B. Straub, P. Fromherz, unpublished results.
- [12] V. Kiessling, P. Fromherz, unpublished results.
- [13] D. Braun, P. Fromherz, unpublished results.
- [14] R. Weis, B. Müller, P. Fromherz, *Phys. Rev. Lett.* **76**, 327 (1996).
- [15] V. Kiessling, B. Müller, P. Fromherz, *Langmuir* **16**, 3517 (2000) .
- [16] P. Fromherz, V. Kiessling, K. Kottig, G. Zeck, *Appl. Phys. A* **69**, 571 (1999).
- [17] G. Zeck, P. Fromherz, *Langmuir*, in press.
- [18] B. Kuhn, P. Fromherz, unpublished results.
- [19] H. Ephardt, P. Fromherz, *J. Phys. Chem.* **97**, 4540 (1993).
- [20] A. Lambacher, P. Fromherz, *J. Phys. Chem.* **105**, 343 (2001).
- [21] D. Braun, P. Fromherz, *Phys. Rev. Lett.* **86**, 2905 (2001).
- [22] S. Vassanelli, P. Fromherz, *J. Neurosci.* **19**, 6767 (1999).
- [23] B. Straub, E. Meyer, P. Fromherz, *Nature Biotech.* **19**, 121 (2001).
- [24] P. Fromherz, *Eur. Biophys. J.* **28**, 254 (1999).
- [25] M. Jenkner, P. Fromherz, *Phys. Rev. Lett.* **79**, 4705 (1997).
- [26] R. Schätzthauer, P. Fromherz, *Eur. J. Neurosci.* **10**, 1956 (1998).
- [27] S. Vassanelli, P. Fromherz, *Appl. Phys. A* **65**, 85 (1997).
- [28] C. Figger, A. Stett, P. Fromherz, unpublished results.
- [29] S. Vassanelli, P. Fromherz, *Appl. Phys. A* **66**, 459 (1998).
- [30] A. Stett, B. Müller, P. Fromherz, *Phys.Rev.E* **55**, 1779 (1997).
- [31] M. Ulbrich, P. Fromherz, *Adv. Mater.* **13**, 344 (2001).
- [32] P. Bonifazi, P. Fromherz, *Adv.Mater.* (2002) in press.
- [33] A. A. Prinz, P. Fromherz, *Biol. Cybern.* **82**, L1-L5 (2000).
- [34] M. Jenkner, B. Müller, P. Fromherz, *Biol. Cybern.* **84**, 239 (2001).
- [35] G. Zeck, P. Fromherz, *Proc. Natl. Acad. Sci. USA* **98**, 10457 (2001).
- [36] P. Fromherz, H. Schaden, T. Vetter, *Neurosci. Lett.* **129**, 77 (1991).
- [37] P. Fromherz, H. Schaden, *Eur. J. Neurosci.* **6**, 1500 (1994).
- [38] M. Merz. P. Fromherz, *Adv. Mater.* **14**, 141 (2002).
- [39] S. Dertinger, P. Fromherz, unpublished results.
- [40] P. Fromherz, *Eur. Biophys. J.* **31**, 228 (2002).
- [41] B. Besl, P. Fromherz, *Eur. J. Neurosci.* **15**, 999 (2002).
- [42] P. Fromherz, *Ber. Bunsenges. Phys. Chem.* **100**, 1093 (1996).

- [43] P. Fromherz, in: *Electrochemical Microsystems Technology*,. Eds. J.W.Schultze, T.Osaka, M.Datta., Taylor and Francis, London, 2002.
- [44] P. Fromherz, *Physik. Blätter* **57**, 43 (2001).
- [45] P. Fromherz, *ChemPhysChem* **3**, 276 (2002).